BEILSTEIN JOURNAL OF NANOTECHNOLOGY

Shaping the future of nanotechnology

Edited by Thies Büscher, Yui Sasaki and Hao Lu

Generated on 23 November 2026, 11:13

Imprint

Beilstein Journal of Nanotechnology
www.bjnano.org
ISSN 2190-4286
Email: journals-support@beilstein-institut.de

The *Beilstein Journal of Nanotechnology* is published by the Beilstein-Institut zur Förderung der Chemischen Wissenschaften.

Beilstein-Institut zur Förderung der Chemischen Wissenschaften
Trakehner Straße 7–9
60487 Frankfurt am Main
Germany
www.beilstein-institut.de

The copyright to this document as a whole, which is published in the *Beilstein Journal of Nanotechnology*, is held by the Beilstein-Institut zur Förderung der Chemischen Wissenschaften. The copyright to the individual articles in this document is held by the respective authors, subject to a Creative Commons Attribution license.

BEILSTEIN JOURNAL OF NANOTECHNOLOGY

Comparative study on 3D morphologies of delignified, single tracheids and fibers of five wood species

Helen Gorges[1], Felicitas von Usslar[2], Cordt Zollfrank[2], Silja Flenner[3], Imke Greving[3], Martin Müller[3], Clemens F. Schaber[1], Chuchu Li[*1] and Stanislav N. Gorb[1]

Full Research Paper

Open Access

Address:
[1]Department of Functional Morphology and Biomechanics, Zoological Institute, Kiel University, Kiel, Germany, [2]TUM Campus for Biotechnology and Sustainability, Technical University of Munich, Straubing, Germany and [3]Helmholtz-Zentrum Hereon, Geesthacht, Germany

Email:
Chuchu Li[*] - cli@zoologie.uni-kiel.de

* Corresponding author

Keywords:
3D models; delignification; tracheid; wood; X-ray nanotomography

Beilstein J. Nanotechnol. **2026,** *17,* 239–250.
https://doi.org/10.3762/bjnano.17.16

Received: 08 October 2025
Accepted: 22 January 2026
Published: 04 February 2026

This article is part of the thematic issue "Shaping the future of nanotechnology".

Associate Editor: K. Koch

© 2026 Gorges et al.; licensee Beilstein-Institut.
License and terms: see end of document.

Abstract

Wood tracheids and fibers exhibit diverse structures and shapes across plant species. The hierarchical structure and composition of cellulose, hemicelluloses, and lignin enables wood to withstand high stress. This structural resilience makes wood a versatile material for applications ranging from construction to advanced composites. However, a detailed understanding of how delignification affects softwood tracheid and hardwood fiber morphology is crucial for predicting material behavior and developing modified wood products. This study investigated the overall structural changes due to delignification, in five wood species, namely, spruce, beech, balsa, Douglas fir, and poplar. It additionally provides detailed morphology of delignified single tracheids and fibers. Scanning electron microscopy was used to compare the morphology between untreated and delignified fibers and tracheids. X-ray tomography enabled us to reconstruct high-resolution 3D models of delignified single tracheids or fibers, providing information on the pit arrangements. Moreover, delignification resulted in facilitated separation of fibers and tracheids and frayed wall appearance. We observed similar tracheid/fiber diameters and wall thicknesses for all five wood species. These findings enhance our understanding of the wood fiber and tracheid structures across species and the effects of delignification. The 3D models provide a valuable resource for (1) understanding interspecies differences of fibers and tracheids, (2) optimizing the use of delignified wood in industrial applications (including bio-based and bio-inspired materials), and (3) physical modeling of wood regarding questions of wood biomechanics and water management.

Introduction

Wood fibers in hardwood and tracheids in softwood play a crucial role in the structure and function of vascular plants, particularly in water conduction and mechanical support [1,2]. They are especially important in gymnosperms, where they serve as primary conduits for water transport, whereas in angiosperms, they function alongside vessel elements, contributing to both axial and lateral water movement by providing strength of the tissue [3,4]. Tracheids are specialized cells that are elongated, hollow, and tapered at both ends, forming an interconnected system that facilitates the transport of water and nutrients from the roots to the aerial parts of the plant [3]. Depending on the species and function, conifer tracheids are generally narrow, with varying diameters (8–80 μm) [5]. Overall, vessels and fibers of angiosperms are less uniform with higher ranges of length than those of gymnosperm tracheids, whereas gymnosperm tracheids have similar diameters [3,6].

An important feature of vessel elements and tracheids is the presence of pits in the cell wall, where water moves between adjacent fibers and tracheids. Pits are distinguished between simple pits and bordered pits, which are surrounded by a thickened rim of wall material [6,7]. Several plants, such as conifers, have a torus–margo structure with a thin, porous mesh-like region (margo) and a thickened central part of the membrane (torus) that is slightly larger than the pit aperture [4,7].

Similar to other plant cells, fibers and tracheids have a primary wall (P) composed of cellulose, hemicelluloses, and pectin that are formed during cell growth [8,9]. Once fully grown, they develop two secondary walls (S1 and S2) and a tertiary wall (T) strongly supplemented by lignin. Apart from the middle lamella (ML) and the primary wall (P), the S2 layer being the thickest of the three main layers (S1, S2, and T), is the most important for mechanical support [1,10,11]. Lignin is present in all layers of the secondary and tertiary wall structure, with varying distribution and concentration across these layers but the highest proportions generally found in the S2 and T layers (spruce earlywood: ML 26.8%, S1 10.4%, S2+T 62.8%; spruce latewood: ML 18.4%, S1 7.9%, S2+T 73.7%) [12,13]. Moreover, lignification plays a key role in preventing cell collapse under high tensile stress or/and inner pressure exerted by the water column during transpiration [8].

Wood delignification is a crucial process in various industries, particularly pulp and paper production, biofuel generation, and the development of advanced wood-based materials [11,14]. This process involves the removal of lignin, which can significantly alter the properties of wood, making it more porous, flexible, and amenable to further processing [11]. Several methods have been employed for wood delignification, including chemical, enzymatic, and biological approaches [11,15,16]. The applications of delignified wood are diverse and expanding; they include, for example, the production of high-quality paper or of nanocellulose with applications in electronics, biomedical devices, and advanced composites [11,14]. Recent research has focused on developing more environmentally friendly and efficient delignification methods [17], as well as exploring novel applications for delignified wood in fields such as energy storage, water purification, and sustainable packaging materials [11,18,19].

Given the high versatility of wood across a wide range of applications [18,20,21], investigating the hierarchical structures in fibers and tracheids across different wood species and treatments is essential. By studying delignified fibers and tracheids, one can gain insights into the specific roles of lignin in maintaining tracheid shape, arrangement, and connections between neighboring cells. This knowledge is valuable for optimizing wood processing techniques, developing new wood-based materials and improving the understanding of wood anatomy and its biological function. By removing lignin, it is now possible to obtain high-resolution 3D models of separated single fibers and tracheids, revealing previously hidden details about pit arrangements and morphological variations across different wood species.

Despite the importance of wood fibers and tracheids in structure and function of wood, detailed 3D models of individual fibers and tracheids have been largely absent from scientific literature. Although previous studies have examined wood anatomy using various imaging techniques, such as X-ray microcomputed tomography in addition to scanning and transmission electron microscopy [22-27], high-resolution 3D reconstructions of single fibers and tracheids across multiple species are lacking. This knowledge gap has limited our understanding of the fine structural details and variations in tracheid/fiber morphology.

Therefore, we compared the morphological differences between the fibers of hardwood and tracheids of softwood of five wood species in this study by observation of the structural differences after delignification. Using X-ray tomography, we were able to build 3D models of single fibers and tracheids. Additionally, we imaged untreated and delignified samples using scanning electron microscopy for measuring fiber and tracheid diameter and wall thickness. The 3D models presented in this study provide novel insights into the tracheid/fiber shape, pit arrangements, and structural changes after delignification at an unprecedented level of detail. These results fill the needs for new wood anatomy research and provide further insights for ap-

plications in computer modelling of mechanical properties of fibers and tracheids and for development of novel bio-inspired materials for the industry.

Material and Methods

Wood samples

Wood samples of five different species were used in this study, namely, spruce (*Picea abies* (L.) H.Karst), beech (*Fagus sylvatica* L.), balsa (*Ochroma pyramidale* (Cav. ex Lam.) Urb.), Douglas fir (*Pseudotsuga menziesii* (Mirbel) Franco), and poplar (*Populus* spp. L.). The wood samples were obtained from a local DIY supplier (Lower Bavaria, Germany). Wood identity was ensured by stereomicroscopical investigation of basic anatomical wood features. The samples were cut according to the main anatomical directions for further use. Care was taken that representative areas for each wood species could be investigated (softwoods: earlywood and latewood regions; hardwood: libriform basic tissue).

Sample preparation

Untreated samples were cut into smaller pieces (1 cm × 1 cm × 1 cm) without further treatment. For the treated samples, prior to delignification, wood was prepared by Soxhlet extraction, as previously reported [28], with minor modifications. The wood samples were treated with two consecutive extractions, first using distilled water and acetone (1:6, v/v, ≥99.5%, Carl Roth, Karlsruhe, Germany), followed by toluene (≥99.5%, Carl Roth) for 24 h each. Afterwards, toluene was washed out by extraction with ethanol for 2 h, and the samples were dried at reduced pressure overnight (15 mbar, 40 °C).

For delignification, the wood specimens were added to a solution of $NaClO_2$ (10% (w/v), AppliChem, Darmstadt, Germany) at 75 °C. The reaction was initiated by the addition of glacial acetic acid (4.0% (w/v), 100% purity, VWR) and maintained at this temperature for 6 h, during which the color of the solution changed from dark brown to yellow. The procedure was repeated once for 8 h to ensure full delignification of the wood, as indicated by the complete loss of color of the specimen. The wood pieces were washed with Soxhlet extraction using distilled water as solvent for 5 h, followed by freezing in liquid nitrogen and subsequent lyophilization overnight (−45 °C, 0.080 mbar, Christ Alpha 2–4 LDplus, Christ, Osterode, Germany).

Scanning electron microscopy

Air-dried wood samples of each of the five species (untreated and delignified) were glued onto metal (SEM) stubs and sputter-coated with a 10 nm layer of gold–palladium (Leica Bal-TEC SCD500, Leica, Wetzlar, Germany). The samples were then visualized using a scanning electron microscope (SEM) Hitachi S-4800 (Hitachi, Tokyo, Japan) at an accelerating voltage of 1.5 kV.

Nanotomography and 3D reconstruction

Single fibers and tracheids were easily mechanically separated from the delignified bulk samples without damaging them using fine tweezers and glued on top of conical sample holders using polyvinyl siloxane (President Light Body, Coltene, Altstätten, Switzerland). The dry fibers and tracheids were imaged (at 22.5 °C and 25% RH) using the X-ray tomography setup at the nanotomography endstation of beamline P05 of PETRA III at Deutsches Elektronen-Synchrotron (DESY). The X-ray beam was monochromatized using a Si(111) double crystal monochromator at an energy of 11 keV with a Zernike phase contrast [29]. An X-ray sCMOS camera (Hamamatsu C12849-101U, Pdet = 6.5 µm pixel size, 2048 × 2048 pixel, 16 bit image depth) with a 10 µm Gadox scintillator was used as the detector. For high-contrast and low-dose imaging, holotomography was applied as the phase contrast technique. Here, a gold Fresnel zone plate with a diameter of 300 µm was used [30]. By varying the sample-to-detector distance, different magnifications with fields of view ranging from 48 × 48 μm^2 to 320 × 320 μm^2 and effective pixel sizes of the raw data from 21.6 nm to 157.3 nm were used. At least two samples of each delignified wood species were scanned, resulting in a total of 35 tomograms. The most representative examples without obvious deformations (16 tomograms: spruce $n = 4$, beech $n = 2$, balsa $n = 4$, Douglas fir $n = 2$, and poplar $n = 4$) were selected for presentation.

The phase retrieval was performed using HoloTomoToolbox [31], while the tomographic reconstruction was performed using the P05 reconstruction pipeline, which is based on tomopy [32], as described earlier [30]. The most representative examples (4× spruce, 2× beech, 4× balsa, 2× Douglas fir, and 4× poplar) were then segmented manually with the brush tool and semi-automated with the magic wand tool using Amira 6.0.1 software (FEI SAS, Lyon, France). The segmented data were further processed in Blender software (Blender Foundation, Amsterdam, Netherlands, https://www.blender.org).

Additional interactive 3D models of two samples for each species are available online with links for each model in Supporting Information File 1.

Estimation of tracheid/fiber diameter and wall thickness

Tracheid/fiber diameter and wall thickness were measured from the nanotomography reconstructions using ImageJ software (version 1.53, National Institute of Health, Bethesda, USA [33]). The raw scans were transferred to ImageJ, and the pixel sizes were set based on the respective effective pixel size of the

scan. Because the diameters differed strongly within and between several wood species, we measured two diameters of each tracheid and fiber, that is, the long and short axes of the lumen from cross section per sample and taking both diameters two times per sample (see Supporting Information File 1, Figure S1). This resulted in spruce: n (number of individual samples) = 8 per diameter; beech: n = 4 per diameter; balsa: n = 8 per diameter; Douglas fir: n = 4 per diameter; and poplar: n = 8 per diameter. Differing sample size resulted from the quality of the scans, as some scans were not of sufficient quality for the purpose of this study. We therefore only worked with the scans with sufficient quality (16 in total).

Moreover, the diameter and wall thickness were additionally measured from SEM images of the untreated and delignified samples (always n = 8 per diameter). For the whole experimental setup and a scheme for the measurements, see Supporting Information File 1, Figure S1.

Statistical analyses were performed using RStudio (version 2024.09.0+375). Since the data was not normally distributed, the median values among the groups were compared using Kruskal–Wallis one-way analysis of variance (ANOVA) on ranks and further pairwise comparisons with Dunn's post-hoc test and Holm's correction, with $\alpha = 0.05$ for each statistical test. Due to the relatively small and varying sample size, we decided to only use the unadjusted p-values for our statistical comparisons [34], but both unadjusted and adjusted p-values, can be found in Supporting Information File 1, Table S1 and Table S2.

Results

Morphologies of untreated and delignified fibers and tracheids of five wood species

SEM images of the samples of each wood species are shown below in Figures 1–5, enabling comparisons between the morphology of untreated and delignified fibers and tracheids. After delignification, the single tracheids/fibers could easily be extracted and prepared for tomography. Using the reconstructed data, we built 3D models of at least two samples for each wood species. The shape of the fibers and tracheids and pit arrangements of each wood species are presented alongside the SEM images of untreated and delignified fibers and tracheids.

In untreated spruce, both earlywood (EW) and latewood (LW) were visible, with tracheids in LW having a smaller lumen than those in EW (Figure 1A, yellow rectangles). Both showed close connections to the neighboring tracheids (Figure 1B). After delignification, the tracheids were separated and spaces between the neighboring tracheids were visible (Figure 1C,D). Moreover, the tracheid walls appeared frayed (Figure 1D,E).

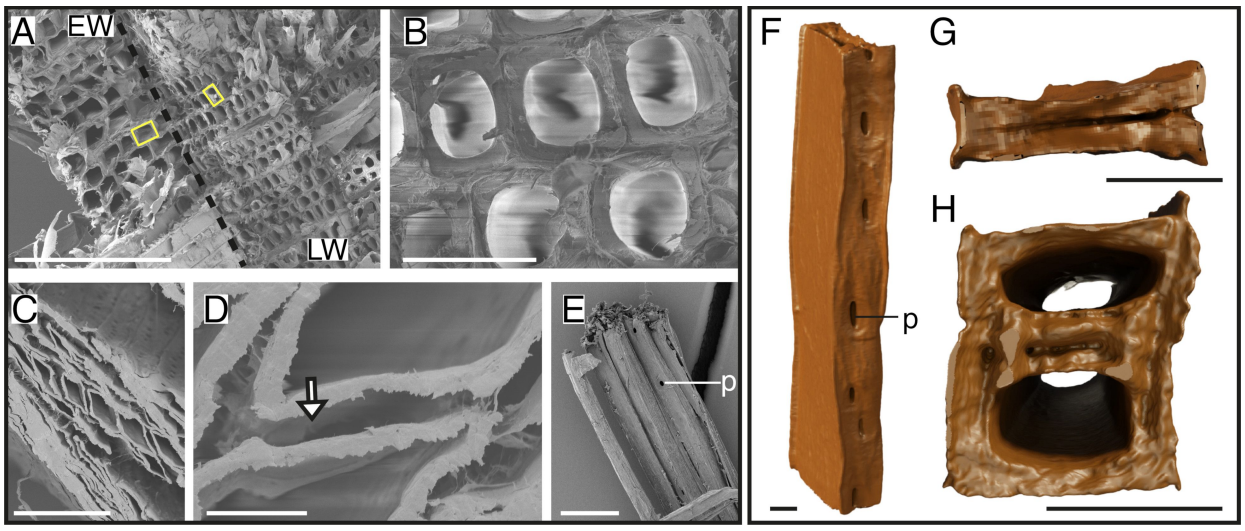


Figure 1: Structure of spruce tracheids. SEM images of untreated and delignified spruce (A–E) and 3D models of delignified tracheids (F–H). Untreated spruce samples (A,B) with larger tracheids (yellow rectangle; EW, left side), smaller tracheids (yellow rectangle; LW, right side), separated with a dotted line (black) (A), and connections between tracheids (B). Delignified spruce samples show a loosened structure (C), spaces between the walls of the tracheids (D, white arrow), and several tracheids with bordered pits (surrounded by a thickened rim of wall material) (E). Single delignified tracheid of LW in longitudinal view with pits on one side (F) and cross sections (G,H), which show the rectangular shape of a single tracheid of LW (G) and two neighboring tracheids of EW (H). Abbreviations: EW – earlywood, LW – latewood, p – pits. Scale bars: A – 300 µm; B – 30 µm; C – 100 µm; D – 10 µm; E – 50 µm; F, G, H – 10 µm.

The tracheid showed a rectangular shape with round lumen in the untreated spruce (Figure 1B), while deformed to rhombus in the delignified spruce. Such deformation was very likely due to the mechanical stress applied on the sample during experimental preparation (Figure 1H). Also, we found rectangular single tracheids with almost no lumen, which were potentially taken from LW areas (Figure 1G). On one side of the tracheid, with a smaller diameter, the pits were arranged longitudinally and in one column (Figure 1F).

Beech fibers showed close connections with the vessels and neighboring fibers in the untreated samples (Figure 2A,B) with bordered pits longitudinally located on one side of the wall (Figure 2C). After delignification, the fibers were more separated, with small spaces between neighboring fiber walls (Figure 2D,E). Similar to the untreated fibers, the delignified fibers exhibited bordered pits on one side (Figure 2F). The fiber had a rectangular/square shape, but less uniform than that of spruce tracheids (Figure 2B,H,I). The pits were longitudinally located on one side of the fiber, with a slightly spiral arrangement (Figure 2G).

In the balsa fiber wood SEM images, we observed two shapes of fibers within a small area of the untreated sample, that is, rectangular and hexagonal ones (Figure 3A). In comparison to fibers, the vessels were larger and had thicker walls (Figure 3B). Similar to beech, the connections between fibers were close in balsa, but the overall wall thickness was smaller (Figure 3C). After delignification, the fibers began to separate from each other and showed spaces between fiber walls (Figure 3D). These spaces were also visible in the longitudinal images of several fibers, which showed bordered pits on the fiber sides (Figure 3E,F). In the tomography data, we found pits on one side of the rectangular balsa fibers (Figure 3G), whereas the hexagonal fibers did not exhibit pits. The 3D models show the same as the SEM images, that is, some fibers had a hexagonal shape (Figure 3H), while others showed a rectangular shape (Figure 3G,I).

Interestingly, untreated Douglas fir samples showed tracheids of different shapes. In one sample, we found rectangular tracheids with a wide lumen (EW), as well as oval and squeezed tracheids (LW) (Figure 4A). Moreover, the inner part of the untreated tracheid wall exhibited a structure with grooves (Figure 4B), which was not observed in delignified tracheids of Douglas fir from both tomography data and SEM images. After delignification, it seemed like the tracheids appeared to change in shape; here, we imaged more oval and bean-shaped tracheids with wide lumina (Figure 4C). Similar to the observations in all other wood species, the connections between the tracheids were lost, resulting in spaces between the tracheids (Figure 4D). In addition to the 3D models, SEM images showed a large number of small pits arranged longitudinally on the tracheids (Figure 4E). Differing from previous species, Douglas fir tracheids had oval or bean shapes, as well as a smaller ratio of tracheid diameter and wall thickness (Figure 4F–H). Besides, the pits of Douglas

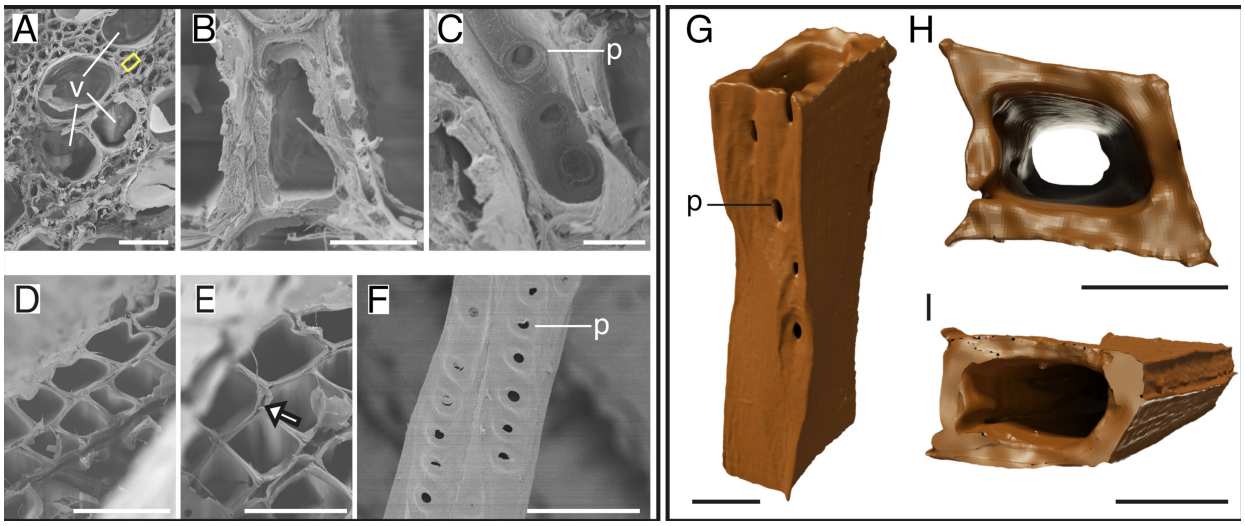


Figure 2: Structure of beech fibers. SEM images of untreated and delignified beech (A–F) and 3D models of delignified fibers (G–I). Untreated beech samples (A–C) with rectangular fibers (yellow rectangles) surrounding the vessels (A), connections between fibers (B), and bordered pits from the inside of the fiber (C). Delignified beech samples showed a loosened structure (D), spaces between the walls of the fibers (E, white arrow), and two fibers with bordered pits (F). Single delignified fiber in longitudinal view with pits on one side (G) and cross-sections (H,I), which show the rectangular/square shape of two beech fibers. Abbreviations: p – pits, v – vessels. Scale bars: A, D, F – 50 µm; B, C – 5 µm; E – 40 µm; G, H, I – 10 µm.

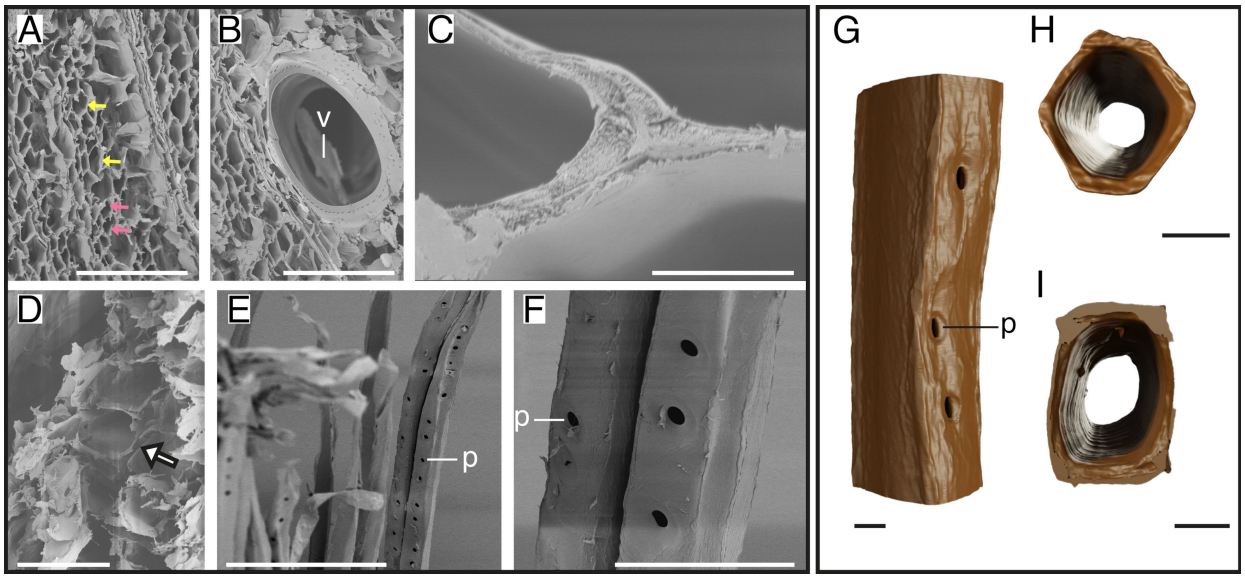


Figure 3: Structure of balsa fibers. SEM images of untreated and delignified balsa (A–F) and 3D models of delignified fibers (G–I). Untreated balsa samples (A–C) with fibers having hexagonal (yellow arrows) and rectangular (pink arrows) shapes (A), fibers surrounding the vessel (B), and close fiber connections (C). Delignified balsa samples show a loosened structure (D) with spaces between the walls of the fibers (white arrow) and fibers with bordered pits (E,F). Single delignified fiber in side view (G) and cross-sections (H,I) showing the hexagonal/rectangular shape of two balsa fibers and pits on one side of rectangular shape (G). Abbreviations: p – pits, v – vessels. Scale bars: A, B, E – 200 µm; C – 5 µm; D, F – 50 µm; G, H, I – 10 µm.

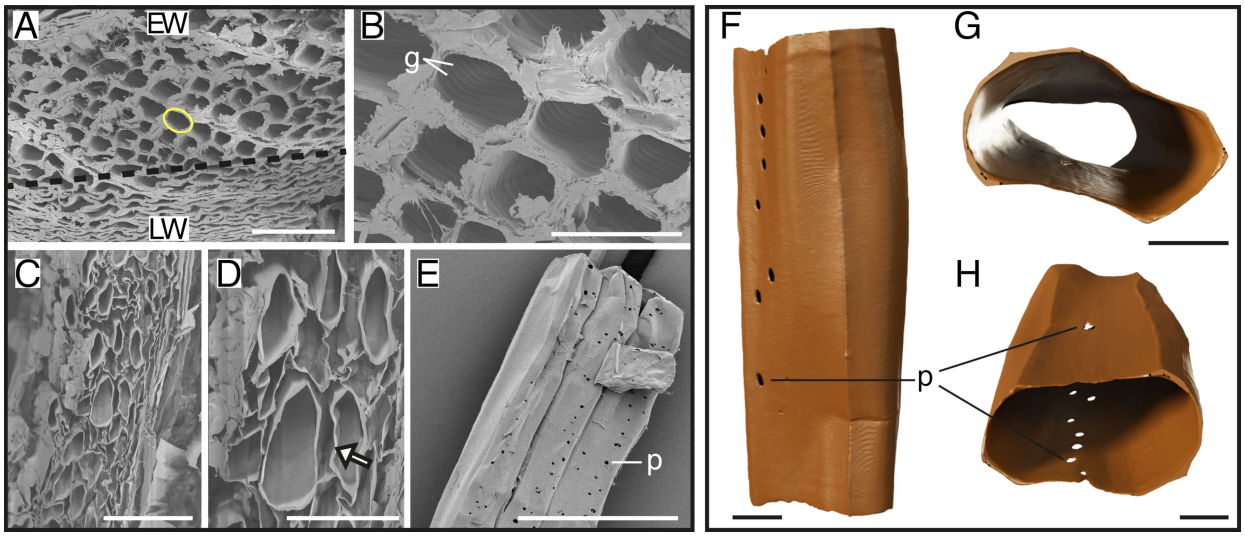


Figure 4: Structure of the Douglas fir tracheids. SEM images of untreated and delignified Douglas fir (A–E) and 3D models of delignified tracheids (F–H). Untreated Douglas fir samples (A,B) with tracheids in compressed (LW, lower part of the picture) and widened (EW, upper + center part of the picture) oval shape (yellow shape) (A), and connections between tracheids with special inner groove structures (B). Delignified Douglas fir samples showed a loosened structure (C) with spaces between the walls of the tracheids (D, white arrow) and tracheids with pits (E). Single delignified tracheid in longitudinal view with pits of EW (F) and cross sections of EW (G,H), which show the oval and bean shapes of two Douglas fir tracheids and pits on two sides (H). Abbreviations: g – grooves, p – pits. Scale bars: A, C, E – 100 µm; B – 40 µm, D – 50 µm; F, G, H – 10 µm.

fir tracheids were smaller and less ordered, and one tracheid had more pits than the fibers and tracheids of other tree species (Figure 4F). In addition, one or maybe two pits were visible on the opposite side (Figure 4H).

Finally, the SEM images of untreated poplar samples showed differently arranged fibers surrounded by vessels (Figure 5A). The small fibers were closely connected to the larger fibers (Figure 5B,C). After delignification, the fibers were strongly

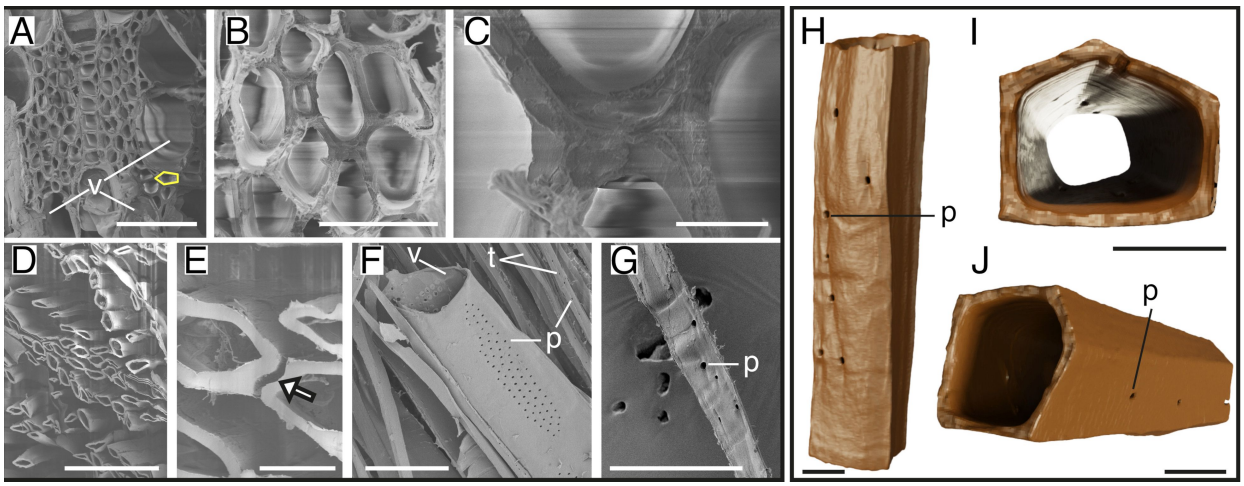


Figure 5: Structure of poplar fibers. SEM images of the untreated and delignified poplar (A–G) and 3D models of delignified fibers (H–J). Untreated poplar samples (A–C) with fibers (one example marked in yellow) surrounded by vessels (A) and connections between fibers of different sizes (B,C). The delignified poplar samples show a strongly loosened structure (D) with various spaces between the walls of the fibers (E, white arrow) and a large vessel with pits (F) as well as a fiber with pits (G). Single delignified fiber in longitudinal view with pits (H) and cross sections (I,J), which show the pentagonal shape of two poplar fibers and pits on one side. Abbreviations: p – pits, t – fibers/tracheids, v – vessels. Scale bars: A, D, F – 100 µm; B – 30 µm; C – 5 µm; E – 10 µm; G – 50 µm; H, I, J – 10 µm.

separated and showed small to very large spaces and connection losses to neighboring fibers (Figure 5D,E). Vessels, which were also separated from fibers, showed bulks of pits on the walls, and neighboring fibers showed pits on the same sides (Figure 5F). In poplar, single fibers showed frayed outer walls, which was presumably due to delignification (Figure 5G). Additionally, an unusual pentagonal shape was observed here (Figure 5H–J). The pits were arranged longitudinally on one side of the fiber (Figure 5H,J).

Comparisons between morphologies of the fibers/tracheids

Because of the different tracheid and fiber shapes, we measured two diameters for each tracheid and fiber, namely, major and minor diameters. Here and below, the length of the long side is the major diameter (diameter 1), while that of the short side is the minor diameter (diameter 2). Since the balsa fiber had two shapes and the hexagonal shape exhibited uniform side length instead of two different lengths, we measured only one diameter for the hexagonal balsa fibers and reported it separately (Table 1). We found that within species, both diameters differed; also, the respective diameters differed after the treatment. For example, both diameters of the oval Douglas fir tracheids differed significantly in untreated and delignified samples (Kruskal–Wallis one-way ANOVA on ranks, $p < 0.0001$; Dunn's post-hoc test, Douglas fir delignified diameter 1 vs diameter 2: $p = 0.0001$, Douglas fir untreated diameter 1 vs diameter 2: $p = 0.0002$; Figure 6A). In delignified spruce and poplar, the diameters differed significantly, as well as in untreated rectangular balsa fibers and untreated poplar (Kruskal–Wallis one-way ANOVA on ranks, $p < 0.0001$; for Dunn's post-hoc test see Supporting Information File 1, Table S1). In addition, we compared the two diameters of untreated and delignified samples between species and found significant differences as well (Table 1, Figure 6A). Douglas fir had the overall largest tracheids among the five species (Table 1, Figure 6A) but showed similar diameters after delignification with a shrinkage of diameter 1 of 4.8% and an expansion of diameter 2 of 38.4%. In poplar, diameter 1 slightly shrunk by 10.7% and diameter 2 slightly expanded by 1.7%. Both diameters of spruce and balsa slightly decreased after delignification with significant differences of diameter 2 in spruce (Kruskal–Wallis one-way ANOVA on ranks, $p < 0.0001$; Dunn's post-hoc test, $p < 0.01$) and with a shrinkage of diameter 1 of 33.3% and of diameter 2 of 63% in spruce. In balsa, diameter 1 shrunk by 22.1% and diameter 2 by 9.4%. In contrast, the diameters of beech slightly increased after delignification, but did not show any statistically significant difference with an expansion of diameter 1 of 26.5% and of diameter 2 of 52.5%. Moreover, diameters 1 of untreated Douglas fir and of untreated spruce were significantly larger than those of untreated beech and poplar (Kruskal–Wallis one-way ANOVA on ranks, $p < 0.0001$; Dunn's post-hoc test, for p-values see Supporting Information File 1, Table S1; Figure 6A). Balsa showed the overall second largest diameters among the species, with a significantly larger diameter 1 of the untreated samples compared to the smallest in beech (Kruskal–Wallis one-way ANOVA on ranks, $p < 0.0001$; Dunn's post-hoc test, $p < 0.001$), directly followed by spruce (Table 1, Figure 6A). The diameters of delignified spruce and of all beech and all poplar samples were in similar ranges (approx-

Table 1: Comparison of the tracheid and fiber morphologies of the studied wood species. Shape, diameter, and wall thickness of the five wood species and the two treatments. Data shows mean ± standard deviation. All untreated samples were *n* = 8, exception: balsa hexagonal *n* = 16. Delignified samples: diameter measurements: spruce and poplar *n* = 16, beech, balsa rectangular and Douglas fir *n* = 12, delignified balsa hexagonal *n* = 24; wall thickness measurements: spruce and poplar *n* = 16, beech and Douglas fir *n* = 12, balsa *n* = 22.

Species	Treatment	Shape	Diameter [µm]		Wall thickness [µm]
			Diameter 1	Diameter 2	
spruce (*P. abies*)	untreated	rectangular	37.2 ± 9.9	27.4 ± 9.9	4.2 ± 0.6
	delignified		29.9 ± 11.4	13.1 ± 8.5	2.2 ± 1.2
beech (*F. sylvatica*)	untreated	rectangular	17.1 ± 2.6	11.3 ± 2.6	1.3 ± 0.4
	delignified		21.5 ± 4.0	16.6 ± 4.2	1.8 ± 0.9
balsa (*O. pyramidale*)	untreated	hexagonal	33.6 ± 8.9		0.8 ± 0.3
	delignified		27.2 ± 5.6		2.4 ± 1.5
	untreated	rectangular	35.8 ± 5.6	23.6 ± 5.9	0.8 ± 0.3
	delignified		29.2 ± 4.6	22.2 ± 3.9	2.4 ± 1.5
Douglas fir (*P. menziesii*)	untreated	oval	44.2 ± 9.2	14.3 ± 4.6	1.5 ± 0.4
	delignified	oval	41.7 ± 6.7	17.9 ± 3.6	1.0 ± 0.5
poplar (*P.* spp.)	untreated	pentagonal	23.2 ± 3.0	14.1 ± 1.8	1.5 ± 0.4
	delignified		20.7 ± 2.1	13.5 ± 5.1	1.6 ± 0.4

imately 13–29 µm; Table 1, Figure 6A). All p-values for statistically significant differences are provided in Supporting Information File 1, Table S1. For the shrinking/expansion ratios of the diameters see Supporting Information File 1, Table S3.

Since the wall thickness was homogenous within the species, we reported only one value for each species and treatment (Table 1, Figure 6B). No significant differences were found in the wall thickness between treatments of most examined tree

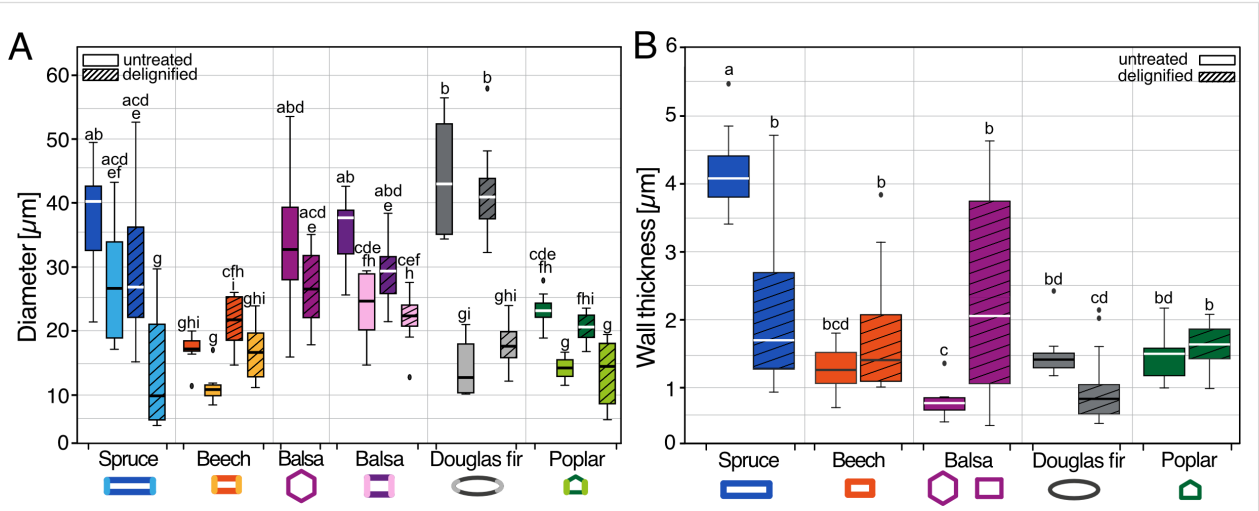


Figure 6: Fiber and tracheid diameter and wall thickness. Two fiber and tracheid diameters (A) of both untreated (plain boxes) and delignified (dashed boxes) wood samples. Diameter 1 in darker colors, and diameter 2 in lighter colors. For hexagonal fibers, only one diameter per treatment is provided, whereas for rectangular balsa, two diameters per treatment are measured. Tracheid and fiber wall thickness (B) of the untreated (plain boxes) and delignified (dashed boxes) wood samples are provided. Kruskal–Wallis ANOVA and Dunn's post-hoc test were used for statistical processing of the data. Different letters indicate statistically significant differences. All statistically significant differences are presented in Supporting Information File 1, Tables S1 and S2. All untreated samples were *n* = 8, exception: balsa hexagonal *n* = 16. Delignified samples: diameter measurements: spruce and poplar *n* = 16, beech, balsa rectangular and Douglas fir *n* = 12, delignified balsa hexagonal *n* = 24; wall thickness measurements: spruce and poplar *n* = 16, beech and Douglas fir *n* = 12, balsa *n* = 22.

species, except for balsa and spruce. In balsa, we observed that delignification significantly increased the wall thickness in comparison to the untreated balsa samples with an expansion of 165.8% (Kruskal–Wallis one-way ANOVA on ranks, $p < 0.0001$; Dunn's post-hoc test, $p < 0.009$; Table 1, Figure 6B). In contrast, the wall thickness significantly decreased in spruce after delignification with a shrinkage of 58.4% (Kruskal–Wallis one-way ANOVA on ranks, $p < 0.0001$; Dunn's post-hoc test, $p < 0.05$; Table 1, Figure 6B). When comparing untreated samples, spruce had overall the highest value for wall thickness and significantly higher than all other wood species (Kruskal–Wallis one-way ANOVA on ranks, $p < 0.0001$; Dunn's post-hoc test, for p-values see Supporting Information File 1, Table S2; Table 1, Figure 6B). Comparing delignified samples, balsa and spruce had a significantly larger thickness than beech, Douglas fir, and poplar (Kruskal–Wallis one-way ANOVA on ranks, $p < 0.0001$; Dunn's post-hoc test, for p-values see Supporting Information File 1, Table S2; Table 1, Figure 6B). All p-values for statistically significant differences are provided in Supporting Information File 1, Table S2. For the shrinking/expansion ratio of wall thickness see Supporting Information File 1, Table S4.

Discussion

The results presented in this study provide distinct insights into the structural differences in wood fibers and tracheids across various species before and after delignification and novel data on high-resolution 3D morphology of single delignified fibers and tracheids. Tracheid and fiber shapes can vary strongly across the five tree species studied. We identified four distinct shapes, namely, rectangular tracheids and fibers in spruce (Figure 1), beech (Figure 2), and balsa (Figure 3), oval tracheids in Douglas fir (Figure 4), pentagonal fibers in poplar (Figure 5), and hexagonal fibers in balsa (Figure 3). The presence of two fiber shapes in balsa sets it apart from the other species, which exhibited only one shape. However, variations in lumen size are evident within softwood, as seen in the smaller lumina of latewood (LW) tracheids and the wider lumina of earlywood (EW) tracheids in both spruce (Figure 1A) and Douglas fir (Figure 4A).

Such variation in lumen size may reflect the evolutionary adaptations of different tree species to specific environmental conditions and their different functional requirements. For instance, larger lumina typically form in earlywood during optimal environmental conditions, while latewood tracheids develop narrower lumina as a response to limited growth resources [35,36]. It seems that larger lumina in earlywood enhance water transport efficiency during growth seasons, enabling the trees to support rapid growth. Conversely, narrower lumina in latewood provide superior mechanical support during periods of reduced growth, ensuring structural stability. However, across the five species studied here, the hardwood fibers, in general, show wider lumina than softwood tracheids. Environmental factors, such as higher environmental temperatures and less compact, well-aerated soils also promote the development of fibers and tracheids with larger lumina [37,38], which very likely result from high evaporation, as well as suitable environmental conditions for growth. In brief, tracheid dimensions are not static; they vary within individual trees or between species and are influenced by multiple factors, including environmental conditions and seasonal growth patterns [37,39].

Using 3D models, we additionally showed pit arrangements of single fibers and tracheids with unprecedented 3D details in spatial distribution compared to traditional methods such as SEM, which, however, show more details of the pit structures [40-42]. Unlike those conventional imaging methods, nano-CT 3D models provide a comprehensive view of pit distribution and spatial organization, enabling a deeper understanding of their role in water transportation and potential mechanical side effects [25-27]. However, due to the small sample size, we can only speculate on the real pit distribution and only show an insight into a small number of 3D-reconstructed fibers and tracheids. To make better conclusions about the pit distribution, a higher sample size and results from several methodologies are needed. In our data, we found that the pits could be located either on only one side of the tracheids and fibers, for example, in spruce (Figure 1), beech (Figure 2), or on multiple sides of the fibers, for example, in balsa (Figure 3) and poplar (Figure 5), which does not correspond with the descriptions of Richter and colleagues [43]. Usually, beech has pits on tangential and radial walls, while fiber pits of poplar appear only on radial walls [43]. In Douglas fir, the pits were generally smaller, more frequent and less ordered compared to the other four species (Figure 4). Moreover, the pit arrangements and distributions vary with tree age and tracheid/fiber characteristics. For instance, in *Pinus radiata*, the number of pits per tracheid is related more to tracheid length in the first ten years of growth, whereas it primarily correlates with wood age [44]. Additionally, tracheid diameter and pit diameter can have a positive linear relationship, with larger fibers or tracheids containing larger pits [44,45]. This complies with our observation when comparing spruce and balsa samples to the poplar samples. The functional implications of pit arrangement for water transportation across species remain unclear. Nevertheless, it is worth mentioning the general climatic backgrounds of the five species as this provides an ecological context for interpreting their wood anatomical features. In general, all five species in this study prefer humid and moist environments. Spruce and beech generally favor cool temperatures and adequate rainfall during growth season [46,47], Douglas fir and poplar perform better

with moderate temperatures, but are able to adapt to various environments [48,49], while balsa trees favor tropical and subtropical climates [50].

Across all wood types studied, delignification results into (1) facile separation of fibers and tracheids with visible spaces between neighboring walls (removal of the lignin-rich middle lamella) and (2) a frayed appearance of tracheid/fiber walls. These observations underline the crucial role of lignin in maintaining the structural integrity and cohesion between fibers and tracheids in wood [51,52]. In contrast to the overall arrangement changes of the wood after delignification, we did not observe significant dimensional changes of the fibers or tracheids. While Bao et al. [53] measured a decrease in wall thickness after delignification, our results showed that the wall thickness remains mostly unchanged after delignification, except for balsa, where wall thickness increased after delignification (Figure 6B). This increase might be due to differences in wood samples and possible discrepancies between EW and LW. The stability of the tracheid/fiber dimensions after delignification suggests that hemicellulose and cellulose may play an important role in maintaining the basic single tracheid/fiber structure after removing lignin [54,55]. This is also reasonable from a materials perspective since the elastic modulus of cellulose is 15 times that of lignin [56,57]. Moreover, lignin might contribute more to the bonding of fibers or tracheids instead of increasing the stability of a single tracheid since the wall thickness remained the same after delignification, but spaces between fibers and tracheids appeared. In addition, gaps between adjacent fibers and tracheids after delignification have also been reported previously [41,43]. Overall, by delignification of the samples and the following nanotomography, we were able to show 3D models of single tracheids and fibers, by easily separating them without further destruction of the tracheids or fibers and whole samples. We were able to show models of neatly separated tracheids and fibers with clean walls. Using nanotomography in combination with delignified samples can improve our understanding of tracheid/fiber and pit distribution of single cells, which was not possible to differentiate and separate in previous tomographical imaging studies [41].

This study represents a high-resolution 3D imaging approach to delignified single fibers and tracheids, paving the way for more effective modeling applications, such as finite element modeling or computational simulations of fluid flow or heat transfer, aiding in development of various industrial applications of delignified wood. Accurate 3D models provide valuable insights into tracheid and fiber morphology, offering implications for wood processing techniques and the development of innovative wood-based materials, including bioinspired materials. This study also holds the potential for shedding light on evolutionary adaptations and taxonomic relationships among species. Still, as the sample size was relatively small, our results show a trend. As wood is a highly variable material depending on the growth conditions, further studies with higher sample sizes could help in verifying those trends or showing discrepancies to samples with differing growth conditions.

In conclusion, this study demonstrates the diverse structural adaptations of wood fibers and tracheids across different tree species and the critical role of lignin in maintaining the wood structure. These findings have implications for understanding wood properties, processing techniques, and potential applications in various branches of industry.

Supporting Information

Supporting Information File 1

Additional experimental data.
[https://www.beilstein-journals.org/bjnano/content/supplementary/2190-4286-17-16-S1.pdf]

Acknowledgements

We thank Esther Appel and Alexander Kovalev for their technical support during the experiments. The upper half of the Graphical Abstract was created in BioRender. Gorges, H. (2026) https://BioRender.com/qgpxmnp. This content is not subject to CC BY 4.0.

Funding

Funding to S. N. G. by the grant GO 995/43-1 and to C. Z. by the grant ZO 113/32-1 from the German Science Foundation (DFG) is acknowledged. The funders took no part in the study design, data collection and analysis, decision of publishing or any preparation of the manuscript. We acknowledge Hereon (Geesthacht, Germany) for the provision of the beamtime, related to the proposal at the Hereon-operated P05 imaging beamline (IBL) at PETRA III (DESY).

Ethics Statement

This study did not involve human participants, live animals, or endangered plant species. All wood samples were obtained from commercially available sources and handled in compliance with institutional and national guidelines.

Author Contributions

Helen Gorges: data curation; formal analysis; investigation; methodology; validation; visualization; writing – original draft; writing – review & editing. Felicitas von Usslar: methodology; writing – review & editing. Cordt Zollfrank: funding acquisi-

tion; methodology; writing – review & editing. Silja Flenner: methodology; writing – review & editing. Imke Greving: methodology. Martin Müller: resources; writing – review & editing. Clemens F. Schaber: conceptualization; data curation; formal analysis; investigation; methodology; validation; visualization; writing – review & editing. Chuchu Li: conceptualization; data curation; formal analysis; investigation; methodology; supervision; validation; visualization; writing – review & editing. Stanislav N. Gorb: conceptualization; funding acquisition; methodology; project administration; resources; supervision; writing – review & editing.

ORCID® iDs

Helen Gorges - https://orcid.org/0009-0008-3600-7673
Felicitas von Usslar - https://orcid.org/0009-0001-5260-4549
Cordt Zollfrank - https://orcid.org/0000-0002-2717-4161
Clemens F. Schaber - https://orcid.org/0000-0002-7475-8899
Chuchu Li - https://orcid.org/0000-0001-5524-828X
Stanislav N. Gorb - https://orcid.org/0000-0001-9712-7953

Data Availability Statement

Data generated and analyzed during this study is available from the corresponding author upon reasonable request. The tomography data were uploaded to Sketchfab. The corresponding URLs are provided in Supporting Information File 1 of the article.

References

1. Plomion, C.; Leprovost, G.; Stokes, A. *Plant Physiol.* **2001,** *127,* 1513–1523. doi:10.1104/pp.010816
2. Sperry, J. S. *Int. J. Plant Sci. (Chicago, IL, U. S.)* **2003,** *164,* S115–S127. doi:10.1086/368398
3. Carlquist, S. *Comparative Wood Anatomy;* Springer Series in Wood Science; Springer Berlin: Berlin, Germany, 2001. doi:10.1007/978-3-662-04578-7
4. Pittermann, J.; Sperry, J. S.; Hacke, U. G.; Wheeler, J. K.; Sikkema, E. H. *Science* **2005,** *310,* 1924. doi:10.1126/science.1120479
5. Pittermann, J. *Geobiology* **2010,** *8,* 112–139. doi:10.1111/j.1472-4669.2010.00232.x
6. Sperry, J. S.; Hacke, U. G.; Pittermann, J. *Am. J. Bot.* **2006,** *93,* 1490–1500. doi:10.3732/ajb.93.10.1490
7. Taylor, T. N.; Taylor, E. L.; Krings, M. Introduction to Vascular Plant Morphology and Anatomy. In *Paleobotany. The Biology and Evolution of Fossil Plants,* 2nd ed.; Taylor, T. N.; Taylor, E. L.; Krings, M., Eds.; Elsevier: Amsterdam, Netherlands, 2009; pp 201–222. doi:10.1016/b978-0-12-373972-8.00007-3
8. Hacke, U. G.; Sperry, J. S.; Pittermann, J. Efficiency Versus Safety Tradeoffs for Water Conduction in Angiosperm Vessels Versus Gymnosperm Tracheids. In *Vascular Transport in Plants,* Holbrook, N. M.; Zwieniecki, M. A., Eds.; Elsevier, 2005; pp 333–353. doi:10.1016/b978-012088457-5/50018-6
9. Ulm, F.-J. Construction: Cellular Materials. In *Encyclopedia of Materials: Science and Technology,* 2nd ed.; Buschow, K. H. J.; Cahn, R. W.; Flemings, M. C.; Ilschner, B.; Kramer, E. J.; Mahajan, S.; Veyssiére, P., Eds.; Elsevier: Oxford, 2001; pp 1570–1574. doi:10.1016/b0-08-043152-6/00280-1
10. Chen, Y.; Su, N.; Zhang, K.; Zhu, S.; Zhu, Z.; Qin, W.; Yang, Y.; Shi, Y.; Fan, S.; Wang, Z.; Guo, Y. *Ind. Crops Prod.* **2018,** *123,* 341–352. doi:10.1016/j.indcrop.2018.06.079
11. Li, J.; Chen, C.; Zhu, J. Y.; Ragauskas, A. J.; Hu, L. *Acc. Mater. Res.* **2021,** *2,* 606–620. doi:10.1021/accountsmr.1c00075
12. Fengel, D.; Wegener, G., Eds. *Wood;* De Gruyter: Berlin, Germany, 1983. doi:10.1515/9783110839654
13. Ruelle, J.; Yoshida, M.; Clair, B.; Thibaut, B. *Trees (Heidelberg, Ger.)* **2007,** *21,* 345–355. doi:10.1007/s00468-007-0128-0
14. Kuznetsov, B. N.; Kuznetsova, S. A.; Danilov, V. G.; Yatsenkova, O. V. *React. Kinet. Catal. Lett.* **2009,** *97,* 295–300. doi:10.1007/s11144-009-0037-x
15. Polowski, N. V.; de Toledo, E. C. V.; Filho, R. M. *IFAC Proc. Vol.* **2006,** *39,* 291–295. doi:10.3182/20060402-4-br-2902.00291
16. Soares, B.; da Costa Lopes, A. M.; Silvestre, A. J. D.; Rodrigues Pinto, P. C.; Freire, C. S. R.; Coutinho, J. A. P. *Ind. Crops Prod.* **2021,** *160,* 113128. doi:10.1016/j.indcrop.2020.113128
17. Frey, M.; Widner, D.; Segmehl, J. S.; Casdorff, K.; Keplinger, T.; Burgert, I. *ACS Appl. Mater. Interfaces* **2018,** *10,* 5030–5037. doi:10.1021/acsami.7b18646
18. Chen, C.; Kuang, Y.; Zhu, S.; Burgert, I.; Keplinger, T.; Gong, A.; Li, T.; Berglund, L.; Eichhorn, S. J.; Hu, L. *Nat. Rev. Mater.* **2020,** *5,* 642–666. doi:10.1038/s41578-020-0195-z
19. Moniruzzaman, M.; Ono, T. *Bioresour. Technol.* **2013,** *127,* 132–137. doi:10.1016/j.biortech.2012.09.113
20. Frey, M.; Schneider, L.; Masania, K.; Keplinger, T.; Burgert, I. *ACS Appl. Mater. Interfaces* **2019,** *11,* 35305–35311. doi:10.1021/acsami.9b11105
21. Song, J.; Chen, C.; Zhu, S.; Zhu, M.; Dai, J.; Ray, U.; Li, Y.; Kuang, Y.; Li, Y.; Quispe, N.; Yao, Y.; Gong, A.; Leiste, U. H.; Bruck, H. A.; Zhu, J. Y.; Vellore, A.; Li, H.; Minus, M. L.; Jia, Z.; Martini, A.; Li, T.; Hu, L. *Nature* **2018,** *554,* 224–228. doi:10.1038/nature25476
22. Brodersen, C. R. *IAWA J.* **2013,** *34,* 408–424. doi:10.1163/22941932-00000033
23. Koddenberg, T.; Militz, H. *Micron* **2018,** *111,* 28–35. doi:10.1016/j.micron.2018.05.004
24. Lautner, S.; Zollfrank, C.; Fromm, J. *IAWA J.* **2012,** *33,* 431–439. doi:10.1163/22941932-90000105
25. Lautner, S.; Lenz, C.; Hammel, J.; Moosmann, J.; Kühn, M.; Caselle, M.; Vogelgesang, M.; Kopmann, A.; Beckmann, F. *Proc. SPIE* **2017,** *10391,* 1039118. doi:10.1117/12.2287221
26. Lautner, S.; Beckmann, F. *Proc. SPIE* **2012,** *8506,* 85060F. doi:10.1117/12.929571
27. Schmelzle, S.; Bruns, S.; Beckmann, F.; Moosmann, J.; Lautner, S. *Adv. Eng. Mater.* **2021,** *23,* 2100235. doi:10.1002/adem.202100235
28. Gürer, U.; von Usslar, F.; Zollfrank, C.; Lieleg, O. *Adv. Mater. Interfaces* **2024,** *11,* 2300669. doi:10.1002/admi.202300669
29. Flenner, S.; Storm, M.; Kubec, A.; Longo, E.; Döring, F.; Pelt, D. M.; David, C.; Müller, M.; Greving, I. *J. Synchrotron Radiat.* **2020,** *27,* 1339–1346. doi:10.1107/s1600577520007407
30. Flenner, S.; Kubec, A.; David, C.; Storm, M.; Schaber, C. F.; Vollrath, F.; Müller, M.; Greving, I.; Hagemann, J. *Opt. Express* **2020,** *28,* 37514. doi:10.1364/oe.406074
31. Lohse, L. M.; Robisch, A.-L.; Töpperwien, M.; Maretzke, S.; Krenkel, M.; Hagemann, J.; Salditt, T. *J. Synchrotron Radiat.* **2020,** *27,* 852–859. doi:10.1107/s1600577520002398
32. Gürsoy, D.; De Carlo, F.; Xiao, X.; Jacobsen, C. *J. Synchrotron Radiat.* **2014,** *21,* 1188–1193. doi:10.1107/s1600577514013939

33. Schneider, C. A.; Rasband, W. S.; Eliceiri, K. W. *Nat. Methods* **2012,** *9,* 671–675. doi:10.1038/nmeth.2089
34. Nakagawa, S. *Behav. Ecol.* **2004,** *15,* 1044–1045. doi:10.1093/beheco/arh107
35. Babos, K.; Vörös, G. *Acta Bot. Hung.* **2001,** *43,* 275–286. doi:10.1556/abot.43.2001.3-4.4
36. Cuny, H. E.; Fonti, P.; Rathgeber, C. B. K.; von Arx, G.; Peters, R. L.; Frank, D. C. *Plant, Cell Environ.* **2019,** *42,* 1222–1232. doi:10.1111/pce.13464
37. Antonova, G. F.; Stasova, V. V. *Trees (Heidelberg, Ger.)* **1993,** *7,* 214–219. doi:10.1007/bf00202076
38. Gebauer, R.; Volařík, D.; Martinková, M. *New For.* **2011,** *41,* 75–88. doi:10.1007/s11056-010-9211-2
39. Bannan, M. W. *Bot. Gaz. (Chicago)* **1941,** *103,* 295–309. doi:10.1086/335043
40. Chukhchin, D. G.; Vashukova, K.; Novozhilov, E. *Plants* **2021,** *10,* 1968. doi:10.3390/plants10091968
41. Koddenberg, T.; Greving, I.; Hagemann, J.; Flenner, S.; Krause, A.; Laipple, D.; Klein, K. C.; Schmitt, U.; Schuster, M.; Wolf, A.; Seifert, M.; Ludwig, V.; Funk, S.; Militz, H.; Nopens, M. *Sci. Rep.* **2021,** *11,* 4574. doi:10.1038/s41598-021-83885-8
42. Roth-Nebelsick, A.; Voigt, D.; Gorb, S. *IAWA J.* **2010,** *31,* 257–267. doi:10.1163/22941932-90000021
43. Richter, H. G.; Dallwitz, M. J. Commercial timbers: descriptions, illustrations, identification, and information retrieval. 2000 onwards. https://www-archiv.fdm.uni-hamburg.de/b-online/wood/english/index.htm.
44. Jinxing, L. *IAWA J.* **1989,** *10,* 53–58. doi:10.1163/22941932-90001111
45. Heady, R. D.; Banks, J. G.; Evans, P. D. *IAWA J.* **2002,** *23,* 339–357. doi:10.1163/22941932-90000309
46. Altman, J.; Fibich, P.; Santruckova, H.; Dolezal, J.; Stepanek, P.; Kopacek, J.; Hunova, I.; Oulehle, F.; Tumajer, J.; Cienciala, E. *Sci. Total Environ.* **2017,** *609,* 506–516. doi:10.1016/j.scitotenv.2017.07.134
47. Petrík, P.; Grote, R.; Gömöry, D.; Kurjak, D.; Petek-Petrik, A.; Lamarque, L. J.; Sliacka Konôpková, A.; Mukarram, M.; Debta, H.; Fleischer, P., Jr. *Forests* **2022,** *14,* 26. doi:10.3390/f14010026
48. Biselli, C.; Vietto, L.; Rosso, L.; Cattivelli, L.; Nervo, G.; Fricano, A. *Plants* **2022,** *11,* 2032. doi:10.3390/plants11152032
49. Case, M. J.; Peterson, D. L. *Can. J. For. Res.* **2005,** *35,* 2743–2755. doi:10.1139/x05-191
50. Borrega, M.; Ahvenainen, P.; Serimaa, R.; Gibson, L. *Wood Sci. Technol.* **2015,** *49,* 403–420. doi:10.1007/s00226-015-0700-5
51. Dai, L.; Wang, J.; Liu, X.-E.; Ma, Q.; Fei, B.; Ma, J.; Jin, Z. *Int. J. Biol. Macromol.* **2022,** *222,* 691–700. doi:10.1016/j.ijbiomac.2022.09.206
52. Donaldson, L. A. *IAWA J.* **2019,** *40,* 645–672. doi:10.1163/22941932-40190258
53. Bao, X.; Yang, M.; Zhu, J.; Xu, H.; Dang, H.; Guo, K.; Long, D.; Guan, X.; Chen, X.; Lin, J. *J. Wood Sci.* **2025,** *71,* 44. doi:10.1186/s10086-025-02214-z
54. Obel, N.; Neumetzler, L.; Pauly, M. Hemicelluloses and Cell Expansion. In *The Expanding Cell;* Verbelen, J.-P.; Vissenberg, K., Eds.; Plant Cell Monographs, Vol. 6; Springer: Berlin, Heidelberg, Germany, 2007; pp 57–88. doi:10.1007/7089_2006_071
55. Peng, F.; Peng, P.; Xu, F.; Sun, R.-C. *Biotechnol. Adv.* **2012,** *30,* 879–903. doi:10.1016/j.biotechadv.2012.01.018
56. Cousins, W. J. *Wood Sci. Technol.* **1976,** *10,* 9–17. doi:10.1007/bf00376380
57. Tashiro, K.; Kobayashi, M. *Polymer* **1991,** *32,* 1516–1526. doi:10.1016/0032-3861(91)90435-l

License and Terms

This is an open access article licensed under the terms of the Beilstein-Institut Open Access License Agreement (https://www.beilstein-journals.org/bjnano/terms), which is identical to the Creative Commons Attribution 4.0 International License (https://creativecommons.org/licenses/by/4.0). The reuse of material under this license requires that the author(s), source and license are credited. Third-party material in this article could be subject to other licenses (typically indicated in the credit line), and in this case, users are required to obtain permission from the license holder to reuse the material.

The definitive version of this article is the electronic one which can be found at:
https://doi.org/10.3762/bjnano.17.16

BEILSTEIN JOURNAL OF NANOTECHNOLOGY

Facile synthesis of platinated DNA nanoparticles with radiosensitizing potential

Leo Sala[*1], Tomas Perecko[2], Antonín Kaňa[3] and Jaroslav Kočišek[*1]

Full Research Paper

Open Access

Address:
[1]Dynamics of Molecules and Clusters Department, J. Heyrovský Institute of Physical Chemistry of the CAS, Dolejškova 3, Prague 182 23, Czech Republic, [2]Department of Cell Biology and Radiobiology, Institute of Biophysics of the Czech Academy of Sciences, Kralovopolska 135, 612 65 Brno, Czech Republic and [3]Department of Analytical Chemistry, University of Chemistry and Technology, Technická 5, 166 28 Prague, Czech Republic

Email:
Leo Sala[*] - leo.sala@jh-inst.cas.cz;
Jaroslav Kočišek[*] - jaroslav.kocisek@jh-inst.cas.cz

* Corresponding author

Keywords:
AFM; cisplatin; DNA nanostructures; radiosensitization

Beilstein J. Nanotechnol. **2026,** *17,* 1117–1127.
https://doi.org/10.3762/bjnano.17.76

Received: 15 April 2026
Accepted: 05 August 2026
Published: 13 August 2026

This article is part of the thematic issue "Shaping the future of nanotechnology".

Guest Editor: T. H. Büscher

© 2026 Sala et al.; licensee Beilstein-Institut.
License and terms: see end of document.

Abstract

DNA nanostructures are promising drug delivery platforms but often suffer from limited structural stability and high production complexity. Cisplatin can cross-link DNA and act as a therapeutic agent, offering a simplified approach to stabilize DNA nanostructures while incorporating therapeutic functionality. Here, we explore cisplatin-mediated compaction of a single-stranded DNA scaffold to form stable nanoparticles and evaluate their potential as radiosensitizers. Cisplatin-induced cross-linking produced compact DNA nanoparticles with size and morphology controlled by mixing ratio and incubation time, reaching maximum loading near a 1:1 cisplatin-to-nucleotide mixing ratio, resulting in 0.28 ± 0.06 bound Pt atoms per nucleotide. The nanoparticles showed high thermal stability with the onset of thermal degradation between 80 and 90 °C and remained structurally stable at 4 °C storage for months. Clonogenic assays in FaDu cells demonstrated radiosensitization, with a dose enhancement ratio of 1.17 ± 0.07 at 10% survival. Cisplatin-mediated cross-linking provides a simple and effective method for producing stable DNA nanoparticles without complex origami assembly. The resulting structures retain the radiosensitizing properties of platinum while offering improved stability and storage characteristics. These platinated DNA nanoparticles represent a promising platform for further development of scalable DNA-based radiosensitizers with high drug loading, monodispersity, stability, and versatility for further functionalization.

Introduction

DNA-based nanomaterials are widely investigated as drug delivery platforms [1-4] because of their inherent biocompatibility [5], low immunogenicity [6], high spatial addressability [7,8], and environmental responsiveness [9]. While DNA self-assembly techniques such as DNA origami allow for the precise arrangement of ligands and functional groups [10,11], these

complex structures often suffer from rapid enzymatic degradation and structural dissociation in physiological environments [12,13]. These stability issues, occurring both in vitro and in vivo, remain a bottleneck preventing the transition from laboratory prototypes to viable clinical applications. Another issue preventing the bench-to-bed translation of DNA-nanostructure-based drug delivery systems is commercial feasibility. While the economics of DNA-based drug delivery systems benefit from novel nanostructure mass-production methods [14] and high achievable loading yields [15], the production complexity of sequence-based DNA nanostructure assemblies as well as regulatory issues persist [16,17].

Cisplatin serves as a primary chemotherapeutic agent for various malignancies [18], yet its clinical utility is frequently limited by high systemic toxicity [19,20] and development of tumor resistance [21]. Because the drug lacks a specific targeting mechanism, it is distributed broadly throughout the body, leading to significant off-target effects in healthy tissues. Effective sequestration of the drug within a delivery vehicle is essential to ensure that the payload is only released upon reaching the lower-pH or enzyme-rich tumor microenvironment [22,23]. DNA nanostructures are highly suitable for this purpose. Our prior research demonstrated that cisplatin can perform a dual role by acting as both the therapeutic payload and a stabilizing cross-linker that reinforces the DNA matrix [24].

Beyond its conventional role in chemotherapy, cisplatin acts as a potent radiosensitizer [25,26] by reacting with low-energy secondary electrons generated during radiotherapy to amplify DNA damage within tumor cells [27,28]. While this dose-enhancement effect is well characterized for free cisplatin [29], the translation of this synergy into DNA-based delivery systems is not yet established. This study investigates whether cisplatin-loaded DNA nanoparticles retain their radiosensitizing efficacy when sequestered within a nanostructured vehicle. Furthermore, this research provides a foundation for exploring the radiotherapeutic potential of other DNA-templated metallized nanostructures [30,31].

Moreover, for situations that do not require intricate shapes (strict distance-dependence of nanostructure decoration), DNA origami may not be the most cost-effective system. Instead of assembling intricate folded structures, we thus utilize only the scaffold and induce compaction through cisplatin-mediated cross-linking. This method produces stable nanoparticles while significantly reducing the amount of synthetic "staple" strands required, thereby lowering production costs. We have optimized the synthesis by systematically varying cisplatin concentration and incubation periods to achieve maximum loading efficiency. Furthermore, we demonstrate the robustness of these nanostructures, confirming both their thermal stability and long-term shelf life in unbuffered environments.

Experimental

Nanoparticle synthesis

Solvent exchange to H_2O was first performed on a 100 nM, 100 µL p7249 scaffold supplied in 10 mM Tris buffer with 1 mM EDTA (Tilibit nanosystems) by centrifugal filtration through 100 kDa molecular weight cut-off Amicon filters three times, each time adding 400 µL of Milli-Q water (Millipore, USA). This stock solution was then mixed with the appropriate concentration of cisplatin solution to achieve the desired mixing ratios. The resulting mixture was then allowed to incubate at the desired reaction times without agitation. A final centrifugal filtration was performed to remove excess cisplatin and purify the platinated DNA nanoparticles. The DNA concentration of the mixtures was estimated by measuring their UV absorbance at 260 nm using a Denovix DS-11 FX+ spectrophotometer. The Pt content measured by ICP-MS was calibrated to the ratio of the absorbances at 230 and 260 nm (A_{230}/A_{260}) showing strong linear dependence above $A_{230}/A_{260} = 0.5$ (Supporting Information File 1, Figure S3). This allows for a faster estimation of Pt loading of platinated DNA nanoparticles.

Agarose gel electrophoresis

Gels with 1% agarose were prepared by dissolving 350 mg agarose (Serva) in 35 mL 0.5× TAE (Sigma-Aldrich) buffer with heating. A 3.5 µL drop of 10,000× SYBR Green I nucleic acid gel stain was added to the warm mixture and mixed thoroughly before pouring the gel in the cast. The gel was then allowed to solidy. The platinated DNA nanoparticle samples were diluted to 6 nM in a 10 µL solution. Two microliters of 6× DNA gel loading dye (Thermo Scientific) was then added to the solution and mixed properly before loading into the gel wells. The gel was then run at 100 V for 35 min at room temperature under 0.5× TAE buffer.

Stability experiments at elevated temperatures and in serum-supplemented buffer

For stability tests at different temperatures, platinated DNA nanoparticle and pure ssDNA scaffold solutions (12 nM) were heated up to the desired temperature (23, 50, 60, 70, 80, and 90 °C) in a heating block and allowed to stay at that temperature for 6 min. The samples were then quickly moved to and stored in an ice bath (4 °C) before analysis. A microliter of the samples was used for atomic force microscopy (AFM) analysis, and the rest was used for agarose gel electrophoresis (AGE) analysis.

For stability tests in a serum-supplemented buffer, platinated DNA nanoparticle and pure ssDNA scaffold solutions were first buffer-exchanged into 1× phosphate-buffered saline (PBS; Carl Roth, pH 7.4) by three rounds of spin filtration using 100 kDa molecular weight cut-off Amicon filters. The final solutions were then prepared by adding fetal bovine serum (FBS; Gibco) to 10% (v/v), along with the appropriate amounts of 10× PBS stock and Milli-Q water to achieve a final composition of 1× PBS and a DNA concentration of 12 nM. Incubations were carried out at different time points ranging from 0 to 24 h, with the longest incubation initiated first to allow for simultaneous analysis by AGE. FBS was added only at the start of each respective incubation time point. AGE was subsequently performed to assess potential degradation of the DNA scaffolds and nanoparticle structures.

Atomic force microscopy

Si substrates (~7 × 7 mm^2) were first plasma-cleaned using a Roplass RPS40+ apparatus. One microliter of the platinated DNA nanoparticle solution (12 nM) was then dripped onto the surface of the plasma-cleaned Si substrate and subsequently added with 15 µL of 10× TAE with 125 mM $MgCl_2$. The resulting droplet was allowed to rest for at least 30 min on the surface before washing it with 1 mL of 50% ethanol solution and finally dried using N_2 gas. Imaging was then performed in air using the Dimension Icon AFM (Bruker) PeakForce Tapping Technology and ScanAsyst probes (40 kHz, 0.4 $N{\cdot}m^{-1}$).

Particle size distribution

Atomic force microscopy (AFM) images of the different samples, acquired over a scan area of 3 × 3 μm^2, were first flattened using the Gwyddion software by applying the following preprocessing steps: automatic data leveling through mean-plane subtraction, row alignment using the median method, and horizontal scar correction. The minimum height value was set to zero, and the color scale was stretched to a range of 0–6 nm to enhance the contrast between the particles and the background. The processed images were then saved and analyzed in ImageJ for particle detection and area measurement. Each image was first converted to an 8-bit grayscale image, after which image segmentation was performed by adjusting the threshold to 70–255. Particles were automatically identified using the "Analyze Particles" function with the circularity parameter set to 0–1, while excluding particles that intersected the image edges. A binary mask was also generated to verify that all particles had been correctly detected. This procedure produced a table containing the projected area of each particle, calibrated in square nanometers according to the image resolution. The equivalent particle diameters were then estimated from the measured projected areas by assuming a circular particle geometry. Finally, a histogram of the calculated particle diameters was generated to obtain the particle size distribution.

Inductively coupled plasma mass spectrometry

The inductively coupled plasma mass spectrometry (ICP-MS) analysis of Pt content in the samples was performed using a NexION 5000 spectrometer (PerkinElmer, USA). Pt stock solution (Astasol®, Analytika Ltd., Czech Republic) with a concentration of 1000 ± 2 $mg{\cdot}L^{-1}$ was used to prepare calibration solutions. All solutions were acidified with nitric acid (Analpure® grade, Analytika Ltd., Czech Republic) and diluted with Milli-Q water (Millipore, USA).

Clonogenic assay

FaDu (#305033, squamous cell carcinoma of the hypopharynx) cell line was acquired from Cytion (Germany). Cells were cultured in RPMI-1640 medium (#21875-091, Gibco, USA) supplemented with 10% FBS (#10270106, Gibco, USA) and 1% penicillin/streptomycin (#LM-A4118/100, Biosera, France). Cells were maintained at 37 °C in a humidified atmosphere with 5% CO_2. Cells were authenticated by the vendor using STR profiling, and all mycoplasma tests were negative. The FaDu cells (700 cells per well in 1.5 mL RPMI media with 10% FBS) were then plated in 6-well plates and allowed to adhere overnight. The cells were treated with either the p7249 scaffold or platinated DNA nanoparticles by replacing the cell medium with that containing 5 nM p7249 scaffold or platinated DNA nanoparticles (equivalent cisplatin concentration of 10 µM). The treated cells were allowed to incubate for 24 h and subsequently irradiated with gamma rays at a dose rate of 1 $Gy{\cdot}min^{-1}$ using a ^{60}Co source (Chisostat, Chirana, Czech Republic). After the irradiation, the medium was replaced by fresh medium to wash off extracellular nanoparticles or scaffold DNA. After two weeks, the colonies were fixed, stained with sulforhodamine B, and then counted by taking photos of the wells using a camera (BASLER, type acA2440-35uc) and counting the colonies by binary image segmentation and particle analysis using the ImageJ software. Image acquisition and particle detection parameters are specified in Figure S4 (Supporting Information File 1). The survival fraction represents the number of colonies grown after each irradiation dose with respect to the unirradiated control within each treatment group. Irradiation was done at doses of 2, 4, and 8 Gy for two independent experiments for the platinated DNA nanoparticles and the scaffold DNA and three independent experiments for the control (cells only) treatment.

The survival fractions (SF, n = 2–3) were plotted as a function of dose and fitted to the linear-quadratic (LQ) model in Python 3.14.2 using the "scipy" package and Equation 1. The fitted α

and β parameters, along with their corresponding standard errors, were obtained from the regression analysis and used to calculate the dose required to achieve 10% survival (D_{10}) according to Equation 2. The dose enhancement ratio (DER) was subsequently calculated as the ratio between the D_{10} value for the control condition (cells only) and that of the corresponding treatment system (platinated nanoparticle or P7249 scaffold), as described in Equation 3. The uncertainty in D_{10} was estimated by propagating the standard errors of the fitted α and β parameters using the first-order error propagation method (Equation 4). The uncertainty in DER was calculated by propagating the uncertainties associated with the D_{10} values of the control and corresponding treatment systems according to Equation 5. The reported uncertainties represent the propagated standard errors of the LQ model fit parameters and provide an estimate of the precision associated with the calculated D_{10} and DER values based on the regression analysis. These uncertainties reflect the confidence in the fitted model parameters and their derived quantities.

$$\mathrm{SF} = e^{-\left(\alpha D+\beta D^2\right)} \tag{1}$$

$$D_{10} = \frac{-\alpha+\sqrt{\alpha^2-4\beta\ln\left(0.1\right)}}{2\beta} \tag{2}$$

$$\mathrm{DER} = \frac{D_{10,\mathrm{control}}}{D_{10,\mathrm{system}}} \tag{3}$$

$$\sigma_{D_{10}} = \sqrt{\left(\frac{\partial D_{10}}{\partial\alpha}\sigma_\alpha\right)^2+\left(\frac{\partial D_{10}}{\partial\beta}\sigma_\beta\right)^2} \tag{4}$$

$$\sigma_{\mathrm{DER}} = \mathrm{DER}\sqrt{\left(\frac{\sigma_{D_{10,\mathrm{control}}}}{D_{10,\mathrm{control}}}\right)^2+\left(\frac{\sigma_{D_{10,\mathrm{system}}}}{D_{10,\mathrm{system}}}\right)^2} \tag{5}$$

Results and Discussion

The nanoparticle design concept and the suggested assembly mechanism are illustrated in Figure 1. The approach is based on the controlled compaction of a circular single-stranded p7249 DNA (isolated from an M13mp18 lac phage vector) scaffold of defined length through cisplatin-mediated cross-linking. The

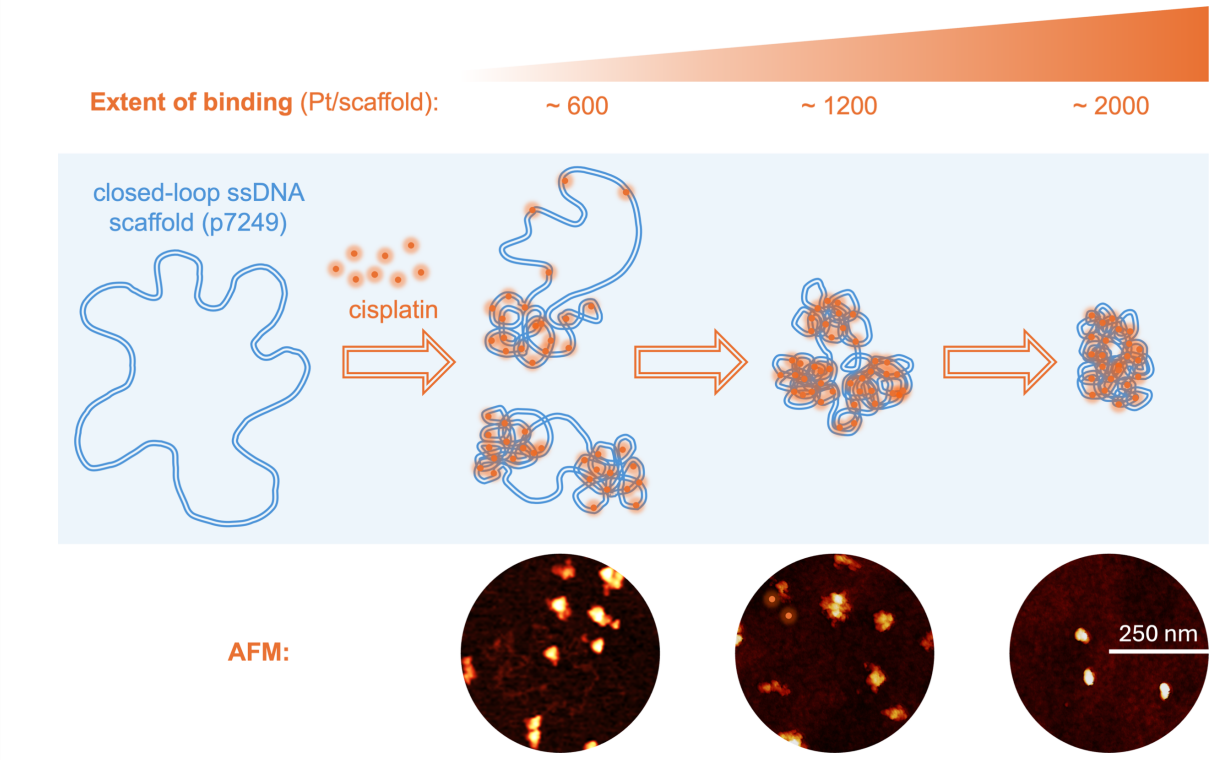


Figure 1: Schematic representation of the proposed platinated DNA nanoparticle assembly. A simplified model illustrates the compaction of the ssDNA scaffold driven by progressive cisplatin-mediated cross-linking, which could be initiated via localized loop formation. The upper panel displays the approximate number of cisplatin molecules bound per nanostructure. The lower panel shows representative AFM images; each circular crop has a radius of 250 nm for scale.

circular ssDNA could be treated as a flexible polymer chain that can potentially undergo a progressive coil-to-globule transition as cross-links are introduced. Typically, the formation of intramolecular cross-links in polymers reduces chain entropy and promotes localized loop formation, which subsequently evolves into a compact, collapsed structure as the cross-link density increases. Utilizing a circular scaffold of fixed length constrains the conformational space of the polymer, which could result in narrower nanoparticle size distributions as opposed to approaches relying on short oligonucleotides or fragmented genomic DNA. This strategy could therefore enable controlled nanoparticle formation through a combination of polymer collapse and cross-linking-driven compaction. The next subsections describe the optimization of the parameters for the synthesis of the platinated DNA nanoparticles, driven by this design concept.

Effect of mixing ratio

The initial cisplatin/DNA scaffold mixing ratios were explored by varying the cisplatin concentration while keeping the scaffold concentration (12 nM) and incubation time constant (16 h). The resulting samples were analyzed by AGE and AFM to determine particle size and distribution. The cisplatin content of purified samples was estimated using the ratio of UV–vis absorbances at 230 and 260 nm (A_{230}/A_{260}) calibrated against ICP-MS measurements of total Pt content of test solutions. Figure 2A shows the particle size distribution derived from 3 × 3 µm AFM images (representative cropped areas are shown in Figure 2D) of particles synthesized at different mixing ratios. A general reduction in particle size is observed as the cisplatin/DNA scaffold ratio increases. However, a transition occurs around a 4000 cisplatin/DNA scaffold ratio, where structures temporarily increase in size before becoming more compact again at 8000 cisplatin/DNA. Both AGE and AFM analyses reveal structural features that help explain this behavior.

In H_2O, with only residual salts from DNA scaffold purification, the DNA scaffold exists primarily in a relaxed form, although collapsed or super-coiled structures arising from secondary interactions may also be present. In Figure 2B, these two forms are evident in the control lane (pure DNA scaffold): The relaxed structure appears as an intense broad band, while the super-coiled form appears as a fainter, higher-mobility band. Both structures are also visible in the AFM image of the control sample, although additional super-coiling may occur due to the presence of divalent salts required for deposition. At cisplatin/DNA scaffold ratios between 1000 and 4000, these bands remain visible. Since all samples were loaded at equal concentrations, the observed decrease in band intensity reflects cisplatin binding, which interferes with intercalation of the nucleic acid stain (SYBR Green I). At these ratios, no significant mobility shifts are observed. However, corresponding AFM images reveal taller and more compact structures, particularly at 2000 and 4000 cisplatin/DNA scaffold ratios.

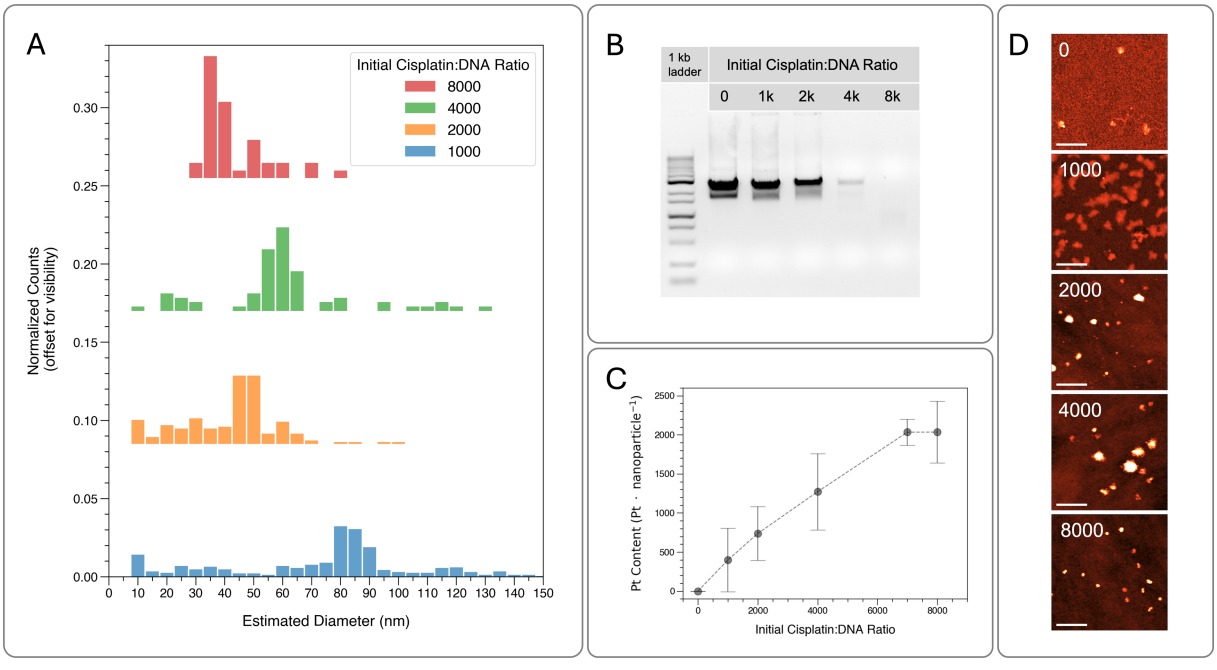


Figure 2: Size dependence on cisplatin concentration. Particle size distribution based on estimated diameters of particles detected in a 3 × 3 µm AFM image (A), AGE micrograph (B), Pt content (C), and representative 1 × 1 µm AFM images, scale bar = 250 nm (D) of platinated DNA nanoparticles synthesized with various cisplatin/DNA scaffold mixing ratios.

Cisplatin cross-links seem to localize within specific regions of the scaffold, forming loop-like structures observed at the 2000 cisplatin/DNA scaffold ratio, while less extensively cross-linked segments remain relatively extended. AFM images of salt-free deposition on a mica substrate (Supporting Information File 1, Figure S6) better highlight these features. Similar formation of small loops has been reported in double-stranded DNA upon cisplatin loading [32]. The smaller apparent particle size distribution compared to the 4000 cisplatin/DNA scaffold ratio is also influenced by limitations in the particle detection method and image resolution, which cannot fully resolve the "free", extended portions of the ssDNA scaffold. As a result, only the condensed looped regions are detected as discrete particles. At a 4000 cisplatin/DNA scaffold ratio, however, these localized loops already appear to occupy most of the scaffold, resulting in the formation of larger clumps. Some of these larger structures may also arise from intermolecular cross-linking between two or more scaffolds or from aggregation induced by substrate interaction or deposition conditions. Increasing the ratio further to 8000 leads to complete structural collapse into more cross-linked, compact nanoparticles. A sketch of the proposed mechanism of scaffold compaction by increasing cisplatin binding/cross-linking is shown in Figure 1.

The band corresponding to the 8000 cisplatin/DNA scaffold ratio in AGE (Figure 2B) is nearly invisible because of a variety of factors that can be associated with the reduced access of the nucleic acid stain through the compact nanostructure for intercalation and possible fluorescence quenching. This band is also observed at a higher mobility, consistent with a more compact structure compared to lower-loading variants. This trend is further supported by the particle size distribution shown in Figure 2A. Consequently, as seen in Figure 2C, maximum compaction and loading can be achieved at an cisplatin/DNA scaffold mixing ratio of approximately 8000, corresponding to 2000 ± 400 bound Pt atoms per nanostructure (0.28 ± 0.06 Pt atoms per nucleotide). The system where the mixing ratio was set to one cisplatin per nucleotide (7200 cisplatin/DNA scaffold mixing ratio) was evaluated; already under these conditions, the maximum loading is achieved after 16 h of incubation.

Effect of incubation time

We used the 2000 cisplatin/DNA scaffold ratio to investigate the effect of incubation time on nanoparticle formation. This ratio was selected because the structures remain visible by gel electrophoresis, enabling easier monitoring, and because it lies below the saturation regime. As expected, compaction increased with incubation time, with particle size decreasing as more time was allowed for cisplatin binding (Figure 3A).

Formation of discrete nanoparticles began at approximately 4 h (Figure 3D), where the cisplatin uptake also begins to slow down (Figure 3C). At 16 h, the AGE results (Figure 3B) still show two bands corresponding to the supercoiled and relaxed states, indicating that the structures remain partially compacted, suggesting localized cross-linked regions and extended loops.

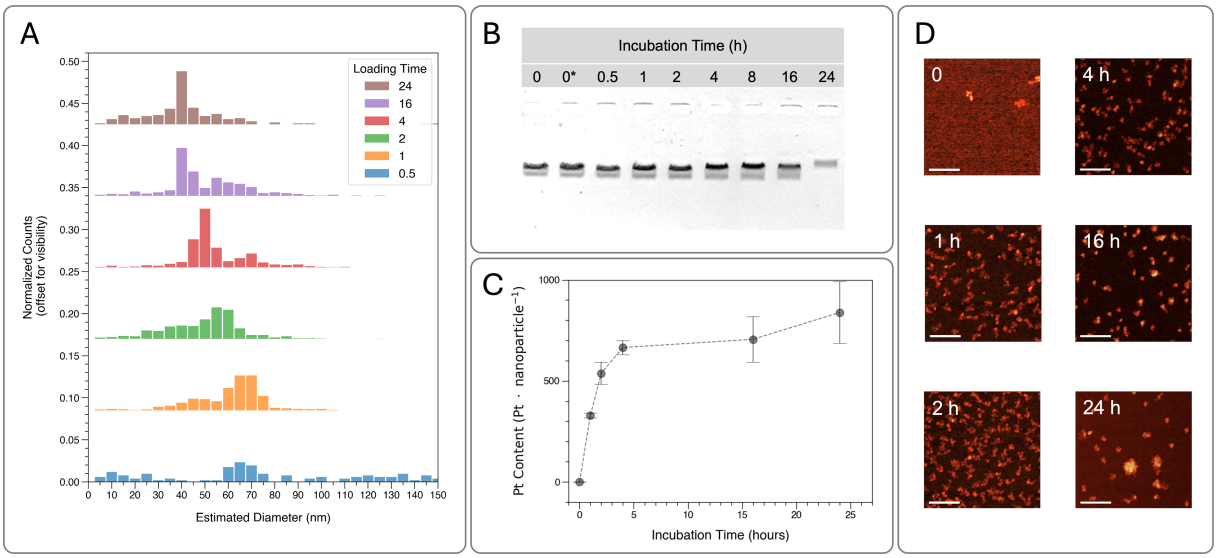


Figure 3: Size dependence on incubation time. Particle size distribution based on estimated diameters of particles detected in a 3 × 3 μm AFM image (A), AGE micrograph (B), and representative 1 × 1 μm AFM images, scale bar = 250 nm (C) of platinated DNA nanoparticles synthesized with different incubation times. In (B), the lane at incubation time 0 corresponds to the pure scaffold without the addition of cisplatin, while 0* represents the sample with cisplatin added immediately before loading into the gel well.

After 24 h, further binding and compaction are observed, albeit some larger structures are present due to agglomeration either in solution or during deposition. It is also worth noting that they reproduce structures similar to those obtained at 4000 cisplatin/DNA scaffold ratio incubated for 16 h.

Stability

To evaluate thermal stability, solutions of platinated DNA nanoparticles (prepared using 8000 cisplatin/scaffold mixing ratio and 16 h incubation time) were heated to temperatures up to 90 °C for 6 min and then quickly quenched in ice to minimize reassembly and drastic conformational changes. The particle size distributions obtained after heating are shown in Figure 4A with corresponding AFM images in Figure 4C. No significant changes in particle size were observed across the temperature range, indicating that the nanoparticles remain structurally intact under elevated temperatures for a few minutes. At 90 °C, however, the size distribution maximum appears slightly skewed toward smaller diameters. This shift may reflect either limitations in AFM resolution at smaller particle sizes or the onset of partial structural degradation. Consistent with this observation, AGE analysis shows a slight mobility shift for samples heated to 90 °C, suggesting minor structural changes at this temperature (Figure 4B). This shift may therefore represent the approximate threshold at which thermal degradation begins to occur.

For comparison, the unmodified DNA scaffold was exposed to the same heating conditions (Supporting Information File 1, Figure S1). In this case, AGE profiles reveal pronounced degradation already at 80 °C in unbuffered solution. The improved thermal stability of the platinated nanoparticles therefore indicate that cisplatin-induced cross-linking and compaction can stabilize the DNA structure up to a certain extent. This enhanced stability exceeds the one typically observed for conventional DNA nanostructures, which generally exhibit lower thermal tolerance under similar conditions [33].

Furthermore, we evaluated the stability of the platinated DNA nanoparticles under near-physiological conditions by incubating them in PBS (pH 7.4) supplemented with 10% FBS at 37 °C for 1–24 h, followed by analysis using gel electrophoresis (Supporting Information File 1, Figure S2). Compared with the free DNA scaffold, which shows evidence of degradation after 1 h of incubation, the gel band corresponding to the platinated DNA nanoparticles shows no detectable smearing or significant loss of intensity throughout the 24 h incubation period, indicating improved stability under these conditions. This could

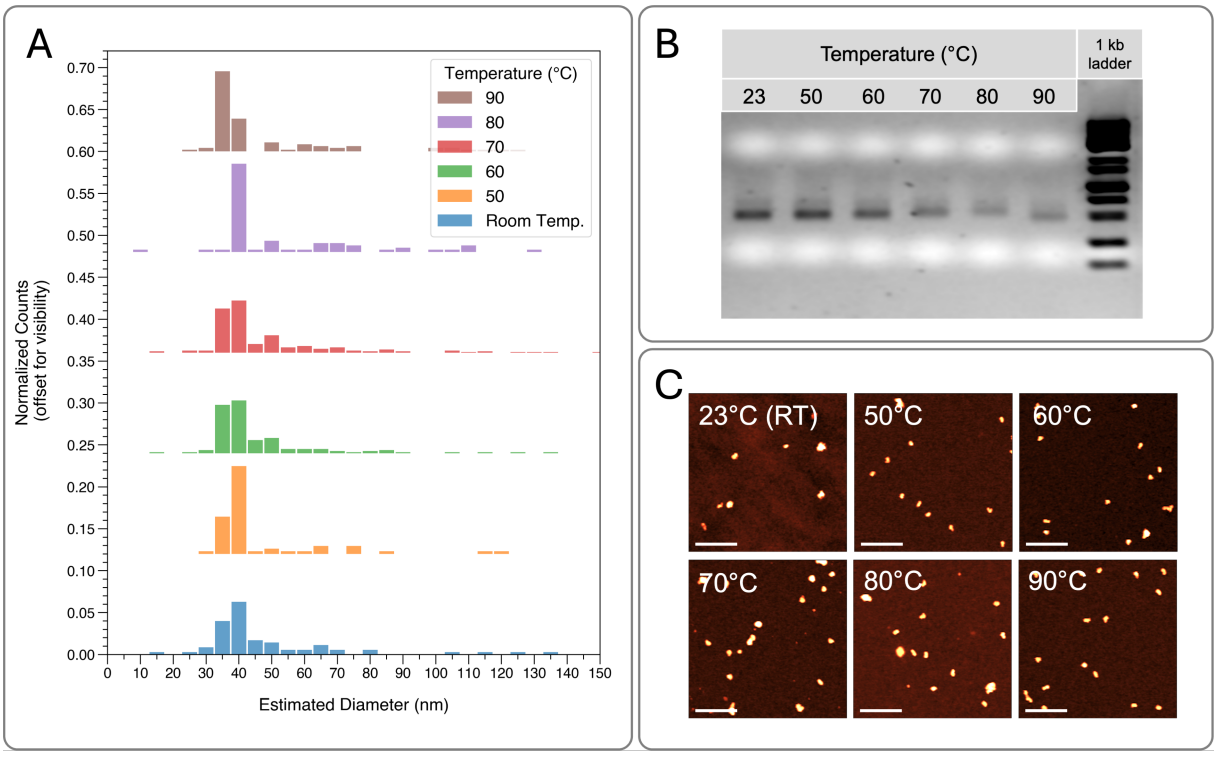


Figure 4: Thermal stability of platinated DNA nanoparticles. Particle size distribution based on estimated diameters of particles detected in a 3 × 3 μm AFM image (A), AGE micrograph (B), and representative 1 × 1 μm AFM images, scale bar = 250 nm (C) of platinated DNA nanoparticles heated to different temperatures from room temp to 90 °C.

extend the application of the platinated DNA nanoparticles for in vitro and in vivo drug delivery explorations.

We also evaluated the long-term stability of the nanoparticles by monitoring particle size and cisplatin content for samples stored in H_2O at 4 °C over a period of two months. AFM analysis (Figure 5A and 5C) revealed minimal changes in particle size distribution throughout the storage period, indicating that the nanoparticles remain structurally stable under these conditions. In addition, the measured variation in cisplatin content remained within the uncertainty of the Pt quantification derived from UV–vis absorption measurements, suggesting negligible loss of bound cisplatin over time (Figure 5B). Collectively, these findings demonstrate good long-term stability of the platinated DNA nanoparticles during storage at 4 °C in aqueous solution, offering a practical storage advantage compared with conventional therapeutic agents.

Radiotherapeutic potential

Platinum-based nanoparticles have been widely investigated as radiosensitizers in radiotherapy, motivating us to evaluate the potential of the platinated DNA nanoparticles in this context. A proof-of-concept radiosensitization assay was employed by using the FaDu cell line, a model for head and neck cancer. Survival fractions were plotted as a function of radiation dose (Figure 6). The resulting survival curves were fitted using the LQ model (Equation 1, Experimental section), where α and β represent the coefficients of the linear and quadratic components and are associated with direct (single-track) and indirect (cumulative) damages, respectively. From these fits, the dose required to achieve 10% survival D_{10} was determined, and the DER was calculated by comparing D_{10} values of treated samples to the cell-only control (Equation 2–Equation 3, Experimental section). The values are listed in Table 1.

The D_{10} values obtained were 7.03 ± 0.13 Gy for the cell-only control, 7.04 ± 0.05 Gy for the free ssDNA scaffold, and 6.03 ± 0.33 Gy for the platinated DNA nanoparticles. The nearly identical D_{10} values for the control and free DNA scaffold indicate that the scaffold itself does not significantly influence radiosensitivity, confirming its suitability as an inert carrier. In contrast, the reduced D_{10} observed for the platinated DNA nanoparticles corresponds to a DER of 1.17 ± 0.07 compared to 1.00 ± 0.02 for the free ssDNA scaffold. This represents an enhancement in radiosensitivity of approximately 10–24%, considering the experimental uncertainty. The ob-

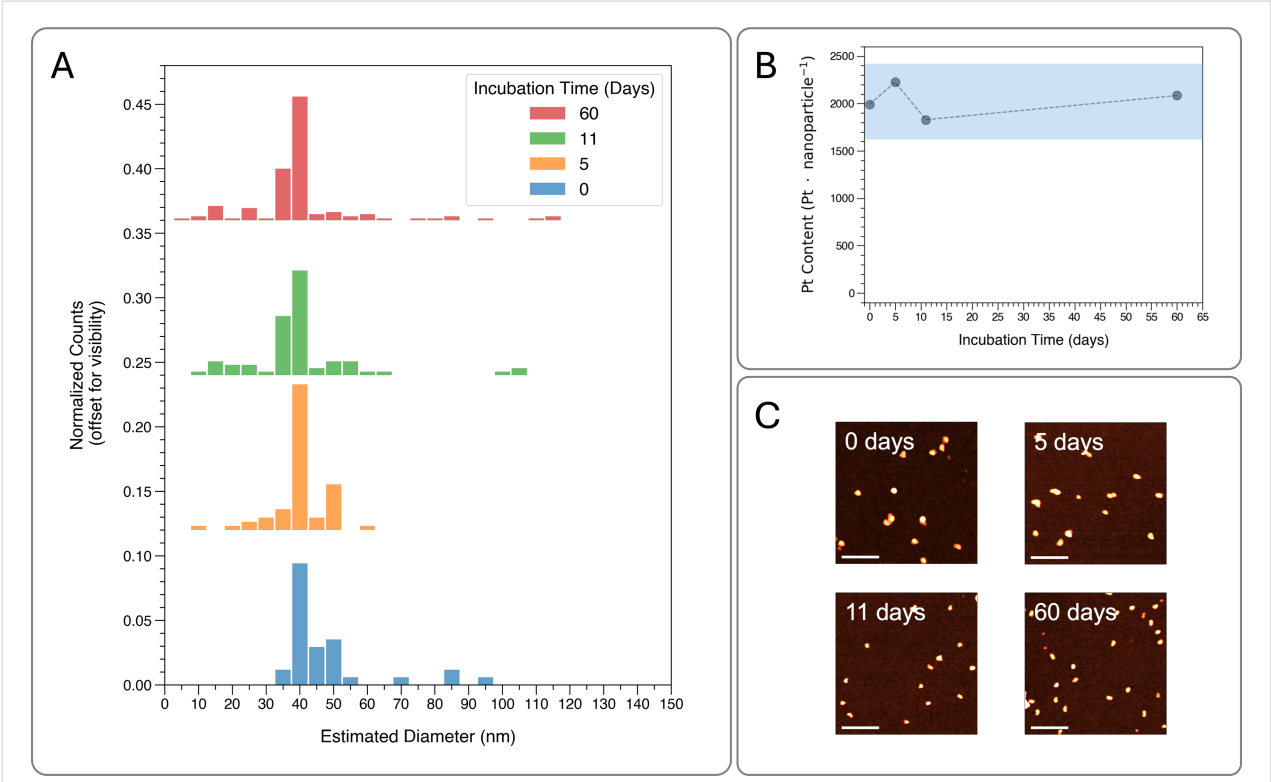


Figure 5: Long-term stability of platinated DNA nanoparticles in refrigerated storage. Particle size distribution based on estimated diameters of particles detected in a 3 × 3 μm AFM image (A), Pt content estimated UV–vis measurements (B), and representative 1 × 1 μm AFM images, scale bar = 250 nm (C) of platinated DNA nanoparticles stored at 4 °C for different durations. In (B), the uncertainty in Pt content measurements derived from UV–vis measurements as calibrated from ICP-MS measurements is shaded in blue.

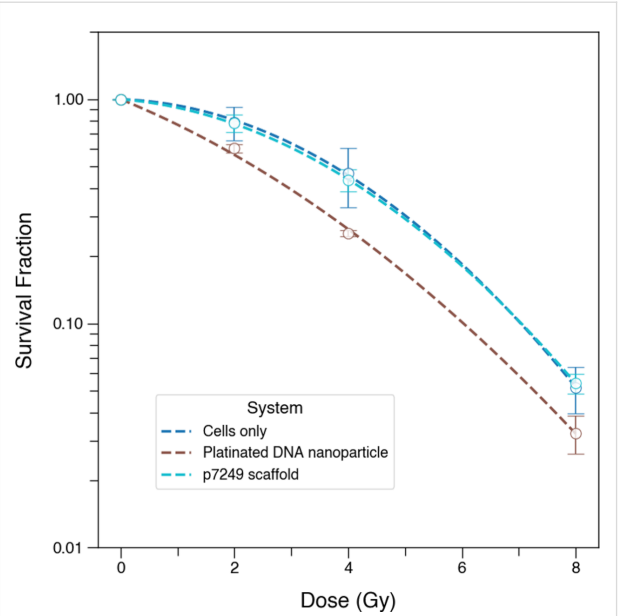


Figure 6: Clonogenic assay. Dose response of colony survival fraction (SF ± SEM) of FaDu cells incubated with platinated DNA nanoparticles (n = 2, brown), p7249 scaffold (n = 2, light blue), or medium only (n = 3, dark blue) for 24 h and then irradiated with gamma rays. Fits following the LQ model (Equation 1) are shown in dashed lines.

served radiosensitization is consistent with the presence of platinum within the nanoparticles, which can increase local energy deposition and enhance radiation-induced DNA damage through secondary electron production and reactive species generation [34]. In FaDu cells irradiated with photon ionizing sources, DER values of approximately 1.20 have been reported for free cisplatin at micromolar concentrations [35]. We have also used the same assay on cisplatin concentrations with limited 10–20% reduction in the cell plating efficiency and observed about 9% DER at 0.2 µM (Supporting Information File 1, Figure S5). The comparable magnitude of radiosensitization observed here using 10 µM cisplatin incorporated within platinated DNA nanoparticles indicates that platinum retains its radiosensitizing functionality when embedded within the DNA nanostructure, while simultaneously benefiting from the structural stability and potential delivery advantages of the nanoparticle platform in this particular cell line and under these irradiation conditions. This modest enhancement may have been influenced by the free, uncross-linked domains acting as radical scavengers, though the nearly identical responses observed in the pure scaffold DNA and control groups suggest this effect was minimal. Additionally, because the cell media were replaced only after irradiation, the observed outcomes likely reflect a combination of both extracellular and intracellular release. Future studies would benefit from exploring cellular uptake, intracellular localization, and the impact of the limited release of coordinately bound cisplatin, all of which may constrain the full radiosensitizing potential of these nanoparticles. Further optimizations could be achieved by tuning nanoparticle concentrations, extending pre-irradiation incubation times to enhance uptake, or employing more active release mechanisms. Nonetheless, these findings indicate that platinated DNA nanoparticles show potential as radiosensitizers and warrant further optimization and systematic investigation.

Conclusion

We demonstrated a simple approach for the synthesis of platinated DNA nanoparticles based on cisplatin-mediated cross-linking of a single-stranded DNA scaffold, which could be potentially scalable due to the use of only a few starting materials. By systematically varying cisplatin-to-DNA scaffold ratio and incubation time, we identified the conditions required for efficient nanoparticle formation and cisplatin loading. Increasing the cisplatin concentration promoted progressive scaffold compaction, with fully collapsed nanoparticles forming near a 1:1 cisplatin-to-nucleotide ratio, representing a remarkable drug load content for the carrier nanoparticle. Time-dependent experiments appeared to be consistent with a nanoparticle formation process involving initial localized cross-linking and eventual scaffold compaction, providing insight into the mechanism of cisplatin-induced DNA scaffold collapse.

The resulting platinated DNA nanoparticles exhibited high thermal stability for a DNA-based material, maintaining structural integrity up to 80 °C, with only minor indications of degradation at the highest temperature tested (90 °C). In contrast to the free DNA scaffold, the platinated DNA nanoparticles showed no degradation after 24 h of incubation in serum-supplemented

Table 1: Parameters (α and β ± SEM) of the dose-response curve fits for the systems studied as well as the calculated effective dose (D_{10} ± SEM) and dose enhancement ratios at 10% survival (DER ± SEM).

Sample	α [Gy^{-1}]	β [Gy^{-2}]	D_{10} [Gy]	DER
control (cells only)	0.020 ± 0.009	0.044 ± 0.001	7.03 ± 0.13	1.00
p7249 scaffold	0.047 ± 0.003	0.040 ± 0.001	7.04 ± 0.05	1.00 ± 0.02
platinated DNA nanoparticles	0.238 ± 0.022	0.024 ± 0.003	6.03 ± 0.33	1.17 ± 0.07
cisplatin (0.2 µM)	0.0628 ± 0.003	0.045 ± 0.001	6.46 ± 0.04	1.09 ± 0.02

physiological buffer. This highlights the stabilizing effect of cisplatin cross-linking. In addition, the nanoparticles demonstrated excellent long-term stability, showing minimal changes in particle size and platinum content after two months of storage at 4 °C in aqueous solution. These findings suggest that cisplatin-mediated cross-linking provides a robust strategy for enhancing the structural stability of DNA-based nanomaterials without the need for complex DNA origami architectures.

Finally, the platinated DNA nanoparticles exhibited some level of radiosensitizing activity in FaDu cells. Compared to untreated controls and free DNA scaffold, the nanoparticles reduced the radiation dose required to achieve 10% survival, corresponding to a dose enhancement ratio of 1.17 ± 0.07. While the observed radiosensitization is moderate, this functionality provides a proof-of-concept for the design of stable DNA-based radiosensitizers. Further optimization may be achieved by systematically investigating parameters such as nanoparticle concentration, incubation time, cellular uptake, and cisplatin release strategies.

Funding

The work was supported by the Ministry of Education, Youth and Sports of the Czech Republic, the European Union via the OP JAK project CZ.02.01.01/00/[0]22_008/0004558 "AMULET", and the Czech Science Foundation project no. 24-11503S.

Conflict of Interest

A patent application (PV 2025-491) partially based on this research has been filed at the Czech Industrial Property Office by the corresponding authors.

Supporting Information

Supporting Information contains AGE/AFM micrographs of the thermal stability assay for the p7249 scaffold, an AGE micrograph of degradation assay in PBS with 10% FBS, the Pt content calibration of ICP-MS and UV–vis measurements, images of colonies evaluated for the clonogenic assay, clonogenic assays of cisplatin controls and cell plating efficiencies, and AFM micrographs of salt-less deposition of platinated DNA nanoparticles on mica.

Supporting Information File 1

Additional experimental data.
[https://www.beilstein-journals.org/bjnano/content/supplementary/2190-4286-17-76-S1.pdf]

Author Contributions

Leo Sala: conceptualization; data curation; formal analysis; investigation; methodology; project administration; validation; visualization; writing – original draft; writing – review & editing. Tomas Perecko: data curation; formal analysis; investigation; methodology; validation; writing – review & editing. Antonín Kaňa: investigation; validation; writing – review & editing. Jaroslav Kočišek: conceptualization; formal analysis; funding acquisition; methodology; resources; supervision; writing – original draft; writing – review & editing.

ORCID® iDs

Leo Sala - https://orcid.org/0000-0003-1091-4386
Tomas Perecko - https://orcid.org/0000-0003-4278-4088
Antonín Kaňa - https://orcid.org/0000-0003-3871-3965
Jaroslav Kočišek - https://orcid.org/0000-0002-6071-2144

Data Availability Statement

Data generated and analyzed during this study is openly available in Zenodo at https://doi.org/10.5281/zenodo.21259520, reference number 21259520.

References

1. Jiang, Q.; Shang, Y.; Xie, Y.; Ding, B. *Adv. Mater. (Weinheim, Ger.)* **2024,** *36,* 2301035. doi:10.1002/adma.202301035
2. Hu, Q.; Li, H.; Wang, L.; Gu, H.; Fan, C. *Chem. Rev.* **2019,** *119,* 6459–6506. doi:10.1021/acs.chemrev.7b00663
3. Safarkhani, M.; Ahmadi, S.; Ipakchi, H.; Saeb, M. R.; Makvandi, P.; Ebrahimi Warkiani, M.; Rabiee, N.; Huh, Y. *Adv. Sci.* **2024,** *11,* 2401617. doi:10.1002/advs.202401617
4. Chen, Y.; Guo, Z.; Li, J.; Wang, K.; Huang, J. *Coord. Chem. Rev.* **2025,** *535,* 216673. doi:10.1016/j.ccr.2025.216673
5. Zhang, Q.; Jiang, Q.; Li, N.; Dai, L.; Liu, Q.; Song, L.; Wang, J.; Li, Y.; Tian, J.; Ding, B.; Du, Y. *ACS Nano* **2014,** *8,* 6633–6643. doi:10.1021/nn502058j
6. Lucas, C. R.; Halley, P. D.; Chowdury, A. A.; Harrington, B. K.; Beaver, L.; Lapalombella, R.; Johnson, A. J.; Hertlein, E. K.; Phelps, M. A.; Byrd, J. C.; Castro, C. E. *Small* **2022,** *18,* 2108063. doi:10.1002/smll.202108063
7. Rothemund, P. W. K. *Nature* **2006,** *440,* 297–302. doi:10.1038/nature04586
8. Knappe, G. A.; Wamhoff, E.-C.; Bathe, M. *Nat. Rev. Mater.* **2023,** *8,* 123–138. doi:10.1038/s41578-022-00517-x
9. Li, S.; Xu, M.; Yao, C.; Yang, D. *Adv. Drug Delivery Rev.* **2025,** *223,* 115610. doi:10.1016/j.addr.2025.115610
10. Udomprasert, A.; Kangsamaksin, T. *Cancer Sci.* **2017,** *108,* 1535–1543. doi:10.1111/cas.13290
11. Jiang, Y.; Zhou, H.; Zhao, W.; Zhang, S. *Anal. Chem. (Washington, DC, U. S.)* **2022,** *94,* 6771–6780. doi:10.1021/acs.analchem.2c00409
12. Keller, A.; Linko, V. *Angew. Chem., Int. Ed.* **2020,** *59,* 15818–15833. doi:10.1002/anie.201916390
13. Ma, W.; Zhan, Y.; Zhang, Y.; Mao, C.; Xie, X.; Lin, Y. *Signal Transduction Targeted Ther.* **2021,** *6,* 351. doi:10.1038/s41392-021-00727-9

14. Praetorius, F.; Kick, B.; Behler, K. L.; Honemann, M. N.; Weuster-Botz, D.; Dietz, H. *Nature* **2017,** *552,* 84–87. doi:10.1038/nature24650
15. Weiden, J.; Bastings, M. M. C. *Curr. Opin. Colloid Interface Sci.* **2021,** *52,* 101411. doi:10.1016/j.cocis.2020.101411
16. Kumar, M.; Jha, A.; Mishra, B. *Chem Bio Eng.* **2024,** *1,* 179–198. doi:10.1021/cbe.3c00023
17. Farooq, M. U.; Lawrie, C. H.; Deng, N.-N. *Adv. Mater. (Weinheim, Ger.)* **2025,** *37,* 2508047. doi:10.1002/adma.202508047
18. Ghosh, S. *Bioorg. Chem.* **2019,** *88,* 102925. doi:10.1016/j.bioorg.2019.102925
19. Tchounwou, P. B.; Dasari, S.; Noubissi, F. K.; Ray, P.; Kumar, S. *J. Exp. Pharmacol.* **2021,** *13,* 303–328. doi:10.2147/jep.s267383
20. Ho, Y.-P.; Au-Yeung, S. C. F.; To, K. K. W. *Med. Res. Rev.* **2003,** *23,* 633–655. doi:10.1002/med.10038
21. Makovec, T. *Radiol. Oncol.* **2019,** *53,* 148–158. doi:10.2478/raon-2019-0018
22. Zhang, Q.; Kuang, G.; Zhang, L.; Zhu, Y. *Biomed. Technol.* **2023,** *2,* 77–89. doi:10.1016/j.bmt.2022.11.011
23. Duan, X.; He, C.; Kron, S. J.; Lin, W. *Wiley Interdiscip. Rev.: Nanomed. Nanobiotechnol.* **2016,** *8,* 776–791. doi:10.1002/wnan.1390
24. Sala, L.; Perecko, T.; Mestek, O.; Pinkas, D.; Homola, T.; Kočišek, J. *ACS Appl. Nano Mater.* **2022,** *5,* 13267–13275. doi:10.1021/acsanm.2c02976
25. Rose, P. G.; Bundy, B. N.; Watkins, E. B.; Thigpen, J. T.; Deppe, G.; Maiman, M. A.; Clarke-Pearson, D. L.; Insalaco, S. *N. Engl. J. Med.* **1999,** *340,* 1144–1153. doi:10.1056/nejm199904153401502
26. Candelaria, M.; Garcia-Arias, A.; Cetina, L.; Dueñas-Gonzalez, A. *Radiat. Oncol.* **2006,** *1,* 15. doi:10.1186/1748-717x-1-15
27. Dong, Y.; Wang, Y.; Zhuang, P.; Fu, X.; Zheng, Y.; Sanche, L. *J. Phys. Chem. B* **2020,** *124,* 3315–3325. doi:10.1021/acs.jpcb.0c00946
28. Sedmidubská, B.; Kočišek, J. *Phys. Chem. Chem. Phys.* **2024,** *26,* 9112–9136. doi:10.1039/d3cp06003a
29. Sousa, L. G.; Edward Bates, J.; Anand, P.; Caudell, J. J.; Colevas, A. D.; Runge, C. L.; Sharon, J. D.; Awan, M.; Beadle, B. M.; Choe, J. H.; Gidley, P. W.; Harari, P. M.; Henson, C.; Katzel, J. A.; Lee, N. Y.; McDowell, L.; Mell, L. K.; Nader, M.-E.; Rudra, S.; Wang, K.; Yang, G.; Yom, S. S.; Wise-Draper, T. M. *J. Natl. Cancer Inst.* **2026,** *118,* 655–668. doi:10.1093/jnci/djaf343
30. Keller, A.; Linko, V. *J. Phys. D: Appl. Phys.* **2026,** *59,* 153001. doi:10.1088/1361-6463/ae5667
31. Kemper, U.; Weizenmann, N.; Kielar, C.; Erbe, A.; Seidel, R. *Nano Lett.* **2024,** *24,* 2429–2436. doi:10.1021/acs.nanolett.3c03751
32. Hou, X.-M.; Zhang, X.-H.; Wei, K.-J.; Ji, C.; Dou, S.-X.; Wang, W.-C.; Li, M.; Wang, P.-Y. *Nucleic Acids Res.* **2009,** *37,* 1400–1410. doi:10.1093/nar/gkn933
33. Hanke, M.; Tomm, E.; Grundmeier, G.; Keller, A. *ChemBioChem* **2023,** *24,* e202300338. doi:10.1002/cbic.202300338
34. Porcel, E.; Liehn, S.; Remita, H.; Usami, N.; Kobayashi, K.; Furusawa, Y.; Sech, C. L.; Lacombe, S. *Nanotechnology* **2010,** *21,* 085103. doi:10.1088/0957-4484/21/8/085103
35. Fang, X.; Sun, P.; Dong, Y.; Huang, Y.; Lu, J. J.; Kong, L. *Front. Oncol.* **2023,** *13,* 896142. doi:10.3389/fonc.2023.896142

License and Terms

This is an open access article licensed under the terms of the Beilstein-Institut Open Access License Agreement (https://www.beilstein-journals.org/bjnano/terms), which is identical to the Creative Commons Attribution 4.0 International License (https://creativecommons.org/licenses/by/4.0). The reuse of material under this license requires that the author(s), source and license are credited. Third-party material in this article could be subject to other licenses (typically indicated in the credit line), and in this case, users are required to obtain permission from the license holder to reuse the material.

The definitive version of this article is the electronic one which can be found at:
https://doi.org/10.3762/bjnano.17.76

BEILSTEIN JOURNAL OF NANOTECHNOLOGY

High-performance graphene/aluminum composites: progress and challenges from an industrial perspective

Shuai GuoLiang*[1], Pan LinXia[2] and Ma HaiLin[3]

Review

Open Access

Address:
[1]Postdoctoral Research Station, Xinjiang Joinworld Co., Ltd., No. 18, Kashi East Road, High-tech District, Urumqi, Xinjiang,China, [2]Xinjiang Chemical Engineering Design Institute, State Power Investment Co. Ltd., No. 559, Kashi East Road, High-tech District, Urumqi, Xinjiang,China and [3]Stevens Institute of Technology, Hoboken, NJ 07030, USA

Email:
Shuai GuoLiang* - shuai_gl@163.com

* Corresponding author

Keywords:
graphene; graphene/aluminum composite; industrial manufacture

Beilstein J. Nanotechnol. **2026,** *17,* 1257–1271.
https://doi.org/10.3762/bjnano.17.86

Received: 12 March 2026
Accepted: 29 July 2026
Published: 14 September 2026

This article is part of the thematic issue "Shaping the future of nanotechnology".

Guest Editor: H. Lu

© 2026 GuoLiang et al.; licensee Beilstein-Institut.
License and terms: see end of document.

Abstract

Graphene/aluminum (Gr/Al) composites are regarded as a promising class of lightweight, high-performance materials for aerospace, automotive, and electronics applications. Graphene's exceptional mechanical, thermal, and electrical properties are integrated with aluminum's favorable density and formability. From an industrial perspective, different methods for producing graphene are analyzed, and graphene/aluminum composites are discussed. The industrialization bottlenecks and path strategies for high-performance Gr/Al composites are analyzed. The major bottlenecks are uniform dispersion of graphene in Al matrix, suppression of the harmful Al_4C_3 interfacial phase, and cost control for large-scale production. The former two problems are addressed by the development of low-cost graphene surface modification technology. The latter problem can be solved by combining different composite technologies, such as spark plasma sintering and casting, which enables excellent microstructure controllability and efficiency. This dual-path framework is provided as a practical reference for the commercialization of Gr/Al composites.

Review

1 Introduction

As an emerging class of lightweight, high-performance materials, graphene/aluminum (Gr/Al) composites have attracted considerable scientific and engineering interest in recent years. Exceptional promise for advanced applications in aerospace engineering, automotive manufacturing, and electronic packaging systems is exhibited by these novel composites [1,2]. Scientific inquiry into these materials began after the seminal findings regarding mechanical graphene exfoliation methodologies in 2004 [3]. The inaugural theoretical investigation concerning graphene/aluminum composites was documented in

2008 and was succeeded by the first experimental validation employing powder metallurgy techniques in 2011 [4,5]. Graphene's extraordinary intrinsic properties, namely, its high theoretical tensile strength (approximately 125 GPa), exceptional thermal conductivity (circa 5000 $W \cdot m^{-1} \cdot K^{-1}$), superior electrical conductivity (approximately $100 \cdot 10^6$ $S \cdot m^{-1}$), and substantial specific surface area (approximately 2630 $m^2 \cdot g^{-1}$), are integrated with aluminum's favorable density characteristics and formability attributes. Thereby, an optimal material solution for structural–functional integration requirements is provided [6-14]. Within the global paradigm of energy transition and sustainable development, raised requirements for lightweight structural components, advanced thermal management solutions, and efficient power transmission/conversion systems in transportation sectors have directly accelerated the rapid advancement of graphene/aluminum-based composite technologies. These composites are established as a research focus in today's materials science [15,16].

Despite their considerable potential, three fundamental technical barriers are encountered in the practical implementation of these composites; these are interfacial bonding and control mechanisms, homogeneous dispersion methods, and the realization of synergistic multiproperty performance enhancement [17-20]. During composite fabrication processes, brittle aluminum carbide (Al_4C_3) phases are frequently generated by interfacial reactions between graphene constituents and the aluminum matrix. The functional role of this interfacial phase remains contentious within the scientific literature: Al_4C_3 is proposed by certain investigations to enhance composite strength through robust interfacial bonding, whereas its propensity to initiate brittle fracture at material interfaces is indicated by alternative studies [21-24]. Then, owing to substantial van der Waals interactions between adjacent graphene layers at the nanoscale, there are significant challenges in achieving homogeneous dispersion within the aluminum matrix. This tendency toward agglomeration readily establishes crack nucleation sites while electron transport and thermal conduction pathways are concurrently impeded [25-27]. Furthermore, performance trade-offs between strength and toughness, strength and electrical conductivity, or strength and thermal conductivity parameters are typically exhibited by conventional composite systems, wherein strength enhancement invariably compromises ductility, electrical conductivity, or thermal transport capabilities respectively [20,22].

A comprehensive "preparation–interface–performance–application" framework is adopted in this review to systematically evaluate recent advances in graphene/aluminum-based composites over the preceding decade. The analysis encompasses preparation methodologies, interfacial engineering strategies, performance characterization methods, and application prospects. Additionally, contemporary academic understanding of interfacial interaction mechanisms and interfacial modification approaches is emphasized, alongside innovative solutions progressively addressing these persistent challenges. Theoretical foundations for future research trajectories and prospective industrial applications are established as the objective.

2 Graphene preparation and dispersion

The performance of graphene/aluminum composites is fundamentally tied to how they are made. Three key aspects are directly impacted by different processing routes, that is, how well graphene is bonded with the aluminum matrix, whether the graphene sheets are spread evenly throughout the material, and what final properties are obtained [1,6,17]. From research and industry experiences, the fabrication can be broken into three stages, namely, graphene is synthesized, it is properly dispersed, and finally the composite is formed [18-20]. The real breakthrough happens when these steps are optimized together rather than separately.

Graphene is the two-dimensional crystalline allotrope of carbon, with the atoms arranged in a honeycomb lattice configuration [9]. Graphene materials are typically classified based on their layer count, structural integrity, and the presence of functional groups or defects [9,27-34]. Single-layer graphene consists of a one-atom-thick carbon lattice, while few-layer graphene refers to stacks of two to ten layers [9,28]. Structural quality is another key criterion; it is distinguished between pristine, defect-free graphene and materials containing vacancies, grain boundaries, or chemical modifications [29-31]. Additionally, graphene derivatives such as graphene oxide (GO) and reduced graphene oxide (rGO) are defined by their oxygen-containing functional groups and subsequent reduction processes [32-34]. The different crystal structures of the three different graphene materials are shown in Figure 1. Precise communication regarding material properties and performance across research and industrial applications is enabled by this systematic classification. These structural attributes and corresponding application domains are comprehensively summarized in Table 1 [9,27-34].

Graphene can be synthesized through a variety of techniques, which are mainly segregated into two conceptual categories, namely, "bottom-up" approaches, wherein atomic precursors are coalesced to form monolayer structures, and "top-down" techniques, wherein bulk graphite is progressively exfoliated into thinner configurations [3,35-38]. Chemical vapor deposition (CVD) is widely employed to produce high-quality, large-area graphene films on metal substrates such as copper or nickel [35]. Alternatively, single-layer graphene flakes are isolated from bulk graphite by mechanical exfoliation, also known as the

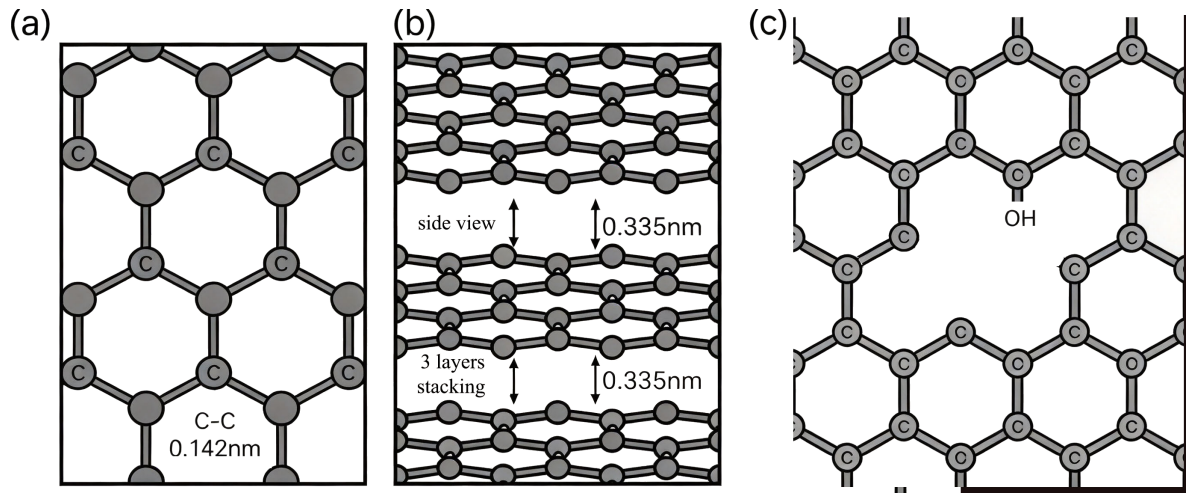


Figure 1: A schematic showing the crystal structure of graphene materials: (a) pristine graphene, (b) three-layer graphene, and (c) reduced graphene oxide.

Table 1: Classification and characteristics of graphene [9,27-34].

Classification	Type	Structural features	Typical applications
layer number	monolayer graphene	single-atom-thick honeycomb lattice (thickness ≈ 0.34 nm)	high-frequency electronics, sensors
	bilayer graphene	AB/AA stacking with interlayer coupling effects	field-effect transistors
	few-layer graphene (3–10 layers)	enhanced dielectric screening, tunable carrier density	energy storage electrodes, composites
	multilayer graphene (>10 layers)	graphite-like properties, reduced conductivity/thermal conductivity	thermal films, structural reinforcements, power transmission
functionalization	graphene oxide (GO)	oxygen-containing groups, hydrophilic, reduced conductivity	biosensor, water purification membranes
	fluorinated/hydrogenated graphene	chemical surface modification for magnetism/hydrophobicity	spintronics, anticorrosion coatings
morphology	film	CVD-grown, superior transparency (>97%) and conductivity	transparent electrodes, flexible displays
	powder	mechanical exfoliation or redox synthesis, high specific surface area (2630 $m^2 \cdot g^{-1}$)	battery additives, supercapacitors
	nanoribbons/quantum dots	edge-dominated quantum confinement effects	quantum computing, optoelectronics

"Scotch tape" method [9]. Additional fabrication routes include liquid-phase exfoliation, where graphite layers are delaminated with the assistance of solvents or surfactants, as well as epitaxial growth on silicon carbide (SiC) substrates [3,36-38]. A versatile toolkit for tailoring the structural and functional characteristics of graphene according to specific application requirements is collectively provided by these methods. Significant variations in defect density, structural characteristics (including charge carrier mobility), and production efficiency/cost parameters are exhibited by graphene produced via these distinct approaches, as systematically documented in Table 2 [3,9,35-38].

Several industrial-scale methods exist for graphene production, including the oxidation–reduction of graphite (redox method) and liquid-phase exfoliation (LPE), each with distinct advantages and limitations. In the CVD technique, metal substrates

Table 2: Performance-cost analysis of main industrial graphene synthesis methods [3,9,35-38].

Method	Key process	Product characteristics	Cost	Industrial maturity
liquid-phase exfoliation (LPE)	water-jet shear peeling	highest quality (defects <0.1%), size <100 μm, layers>10 in generally by LPE	low by LPE	mass production by LPE
redox method	Hummers' oxidation + chemical reduction	oxygen residues (C/O≈8:1), conductivity 10^2 S/m	low	mass production
CVD	CH_4 decomposition on Cu/Ni (1000 °C)	large-area (square meter scale), mobility >4000 $cm^2 \cdot V^{-1} \cdot s^{-1}$	medium (film)	pilot-scale
SiC epitaxy	SiC annealing (>1400 °C)	transfer-free but nonuniform thickness	high	research and development

are exposed within a reaction chamber to hydrocarbon gases and hydrogen at elevated temperatures. Carbon atoms are decomposed from the gas precursors and are crystallized into a graphene film on the metal surface [35]. A critical subsequent step involves transferring the graphene material from the growth substrate, and challenges in production efficiency occur. Therefore, the redox method of graphite was developed, in which graphite is chemically oxidized using strong acids and oxidants to produce GO. GO is hydrophilic, and its dispersion and processing in aqueous solutions are facilitated. The graphene structure is subsequently restored by reduction (via chemical agents or thermal treatment), yielding reduced graphene oxide. However, residual defects and oxygen functionalities are typically contained in rGO, and its mechanical and electrical properties are compromised compared to CVD graphene [32-34,39]. The initial mechanical exfoliation is the original Scotch tape method, in which layers are mechanically cleaved from bulk graphite [9]. While instrumental for fundamental research, it suffers from extremely low yield and poor scalability, which render it unsuitable for industrial manufacturing. LPE was subsequently developed as a mechanical exfoliation method. Graphite powder is dispersed in specific solvents or surfactant solutions. High-energy input, such as ultrasonication or shear mixing, is applied to exfoliate graphite into graphene flakes. While potentially scalable, precise control over flake size and thickness (number of layers) is difficult with LPE, and post-processing is often required to concentrate the material [40].

Redox method and LPE are also the two main industry methods. rGO is the current mainstream industrial product for graphene as its preparation process has matured to relatively low requirements regarding equipment, leading to low cost. However, strong acids and strong oxidants are required for its preparation, resulting in a large number of defects in the obtained graphene and environmental pollution. In addition, its precursor graphene oxide possesses excellent hydrophilic dispersibility coupled with mature process technology and high batch consistency, which enable good manufacturability. Graphene obtained via LPE has an intact crystal lattice and few defects, with a yield second only to that of rGO. However, size and thickness distributions of the exfoliated sheets are difficult to be controlled, and high requirements on post-treatment are imposed by large-scale production, making it more suitable for functional applications with extremely high quality requirements. Key challenges across these methods include balancing production cost, achieving high material quality (e.g., low defect density and large domain size), and ensuring consistent layer control, as shown in Table 3 [38-44].

Recent breakthroughs in graphene dispersion techniques range from ultrasound applications to cryogenic techniques and self-assembly [44-46]. GO clusters were dispersed by Wang et al. [45] using high-frequency sound waves. When just 0.3 wt % of the obtained GO was mixed into aluminum, a 62% jump in strength was shown. Han et al. [46] used a cold environment of 193 K in which graphene sheets were stopped from folding and stacking. With a 10:1 ball-to-powder ratio and 300 rpm rotation speed, graphene stacks only five atoms thick were obtained while the cold welding problem was avoided. Yang et al. [47] made use of electrostatic forces, and graphene was neatly arranged onto aluminum powder. After hot-pressing, a layered structure was developed by the composite, almost like mother-of-pearl. With only little added graphene (0.083 vol %), the material gained strength without sacrificing its stretchiness, which is still over 20% elongation after fracture. From the perspective of industry and production, the selection of graphene for graphene/Al composites requires a comprehensive balance among cost, performance, dispersion process, and interfacial compatibility with the matrix. Reduced graphene oxide and graphene from LPE are the most suitable materials for general application. Reduced graphene oxide is currently regarded as

Table 3: Comparison of redox reduction and liquid-phase exfoliation in terms of efficiency, structural characteristics, and applicable scenarios [38-44].

Parameter	Redox method	Liquid-phase exfoliation
production rate	0.27–0.42 tons per day for the single-line production capacity	up to 0.4 tons per day for the single-line production capacity
defect rate	relatively high (residual oxygen-containing functional groups)	extremely low (preservation of complete sp^2 structure)
structural characteristics	surface with wrinkles and topological defects	multilayers, thickness control requires centralized post-processing.
applicable scenarios	low-cost batch production	high-performance composite materials (such as power transmission and heat dissipation)
cost	88–147 US$/kg for few-layer graphene	~250 US$/kg for few-layer graphene

one of the most promising reinforcing materials for mass production. However, its laminar structure contains abundant defects and oxygen-containing functional groups; while these features are beneficial for chemical modification and interfacial bonding, electrical and thermal conductivity are significantly impaired, which limits applications of rGO.

Graphene obtained via LPE has an intact crystal lattice and excellent intrinsic electrical and thermal conductivity, but it suffers from a wide layer-number distribution. Also, it is more expensive than rGO, making it more suitable for application scenarios with high functional requirements, such as conductive and heat-exchange composites. In terms of layer number selection, the best theoretical strengthening effect can be achieved with single-layer or few-layer graphene, which are expensive, highly prone to agglomeration in matrix composites, and more likely to react with aluminum at high temperatures to form Al_4C_3, by which interfacial strength is deteriorated. Our practical research shows that a good balance between strengthening efficiency and dispersion uniformity can be achieved by the selection of multilayer graphene with a thickness of 2–20 nm. Intense interfacial reactions are avoided, and strength and electrical/thermal conductivity are improved via grain boundary pinning and load-bearing effects.

In addition, to improve the bonding between graphene and aluminum melt and to control interfacial products, rGO can be modified with copper, nickel, or titanium. Also, graft modification can be conducted using the oxygen-containing groups of rGO; thus, agglomeration is reduced and the formation of harmful carbides is inhibited.

Therefore, in current industrial routes, cost-controllable rGO with modification treatment is preferred for mechanically reinforced composites. For products requiring both high electrical conductivity and high thermal conductivity, few-layer or multilayer graphene prepared by mechanical methods may be used, and uniform distribution is achieved via process optimization after surface alloying.

3 Gr/Al composite fabrication methods

3.1 Conventional fabrication methods

Several techniques are involved in the fabrication of graphene/aluminum composites. Each technique brings distinct benefits for structure control, production scaling, and performance boosting. Key problems are tackled by these approaches, including uniform graphene distribution and strong interfacial bonding, through smart engineering solutions. Currently, leading industrial techniques are broadly categorized into solid-state and liquid-phase categories [38,48-52].

Solid-phase methods dominate graphene/aluminum composite manufacturing. Mechanical energy is used to mix graphene into the aluminum matrix. A big advantage is found in the lower working temperatures and controllable reactions at the interface [53]. These features make those methods well suited for parts that need fine grains and high density. Spark plasma sintering (SPS) and accumulative roll bonding (ARB) are the core techniques here. Sufficient flexibility is provided for handling different starting materials and performance targets [24,48-52].

SPS works by first anchoring graphene nanoplatelets (GNPs) onto aluminum powder using high-energy ball milling. Pulsed electric currents are then applied during sintering to create heat and pressure. This fast process densifies the material at surprisingly low temperatures (well below aluminum's melting point) in just 5–10 min [24,49]. Because of the short processing time, grains cannot grow large. Ultrafine grains smaller than 1 μm average result [24]. Nearly full density (>99.2%) with very little remaining porosity (0.56–0.75%) can be achieved by SPS at 500 °C using proper milling time (10 h) and pressure (20–50 MPa) [53]. However, SPS is not perfect. Its equipment is pricey and part size is limited. Special power supplies and vacuum setups are needed for SPS equipment, costing three to

five times more than standard hot presses. Part size is also constrained by the mold design and current flow uniformity. Currently, SPS parts (such as ceramic) up to 100–300 mm can be made by industry, but their shape (aspect ratio) is limited, usually to 2:1 or less [54].

ARB takes a different route. Layers of aluminum foil are stacked with graphene oxide sprayed in between, then rolled together. Typically, a GO/water mixture is sprayed onto the aluminum foil, and 5–8 layers (each 0.1–0.3 mm thick) are stacked. After cold rolling, the thickness is reduced by 50–70% [55-58]. and a layered structure has formed. The intense shear during rolling (reaching 5–8%) helps align the GO along the aluminum grain boundaries. The yield strength of Al6061 is boosted to 320 MPa (a 65% increase) by adding just 0.2 wt % GO this way. Reasonable stretch (12% elongation) is kept, and fracture toughness is improved to 28 $MPa{\cdot}m^{1/2}$. Grain refinement is also achieved by ARB (the grain boundary area is tripled), and GO acts as a barrier. Together, the corrosion rate in salt water (3.5% NaCl) is decreased down to 0.0859 mm per year, an 89% drop compared to the matrix alloy [55]. However, ARB has its own challenges, including interfacial waviness and edge cracking. Bonding strength can vary a lot across the interface if the rolling temperature is not steady [56-58]. Precise temperature control systems, like infrared feedback loops, are often needed for this reason [59]. Also, microcracks tend to form at the edges if the rolling layers are too much in one pass (over 75% reduction). Laser trimming is usually required to fix this and decrease material losses.

Liquid-phase processing provides essential pathways for fabricating Gr/Al composites. Graphene is dispersed directly within molten metal by these methods, enabling large-scale production of complex-shapes. Energy use is cut by 30–40% compared to solid-state approaches, and near-net-shape forming is supported. Two main techniques dominate, namely, semi-solid electromagnetic stirring and conventional stir casting. Each fits different production requirements [17,19,26,60-64]. Semi-solid electromagnetic stirring combines ball milling with magnetic fields. Alternating magnetic fields, usually 30–60 Hz, generate Lorentz forces, and eddy currents create shear rates of 50–100 s^{-1} [62-64]. Graphene clusters are broken up uniformly by this mechanism. Andilab et al. [62] successfully prepared GNP/A319 aluminum alloy composites using ultrasonic-assisted semi-solid casting. The ultimate tensile strength, yield strength, and elongation were enhanced by 10%, 11%, and 32%, respectively, by the addition of 0.05 wt % GNPs. Uniform distribution of GNPs within the aluminum matrix with favorable interfacial bonding was revealed by SEM observations, with no significant agglomeration or Al_4C_3 phase formation. The strengthening mechanism was primarily attributed to the Hall–Petch effect, followed by coefficient of thermal expansion mismatch and load transfer [62]. Furthermore, high scalability potential is demonstrated by this process. Continuous production rates exceeding 200 $kg{\cdot}h^{-1}$ are enabled by multistation electromagnetic stirring systems. The critical challenges of this method involve porosity control and parameter sensitivity management. Gases are easily trapped by melt turbulence, causing 1.8–3.5% porosity without vacuum ($\leq 10^{-2}$ Pa) or hot isostatic pressing (HIP) treatment, far above standard casting's 0.5% [62-64]. Besides, graphene distribution is disrupted by power fluctuations without precise PID control.

The stir casting process incorporates rapid mechanical mixing of graphene into molten aluminum (680–720 °C) using rotating impellers, followed by conventional casting operations. Equipment investment approximately one-fifth that of electromagnetic stirring systems is required by this methodology, making it suitable for small-to-medium batch production scenarios [27,60,61]. However, poor graphene wettability in molten aluminum environments promotes agglomeration under limited mechanical shear conditions. Agglomerate dimensions frequently reach 20–50 μm at 1 wt % GNP incorporation levels, reducing composite elongation to 40% of the matrix alloy value [65]. Additionally, Al_4C_3 formation (content up to 2.1 vol %) is promoted by elevated processing temperatures (>700 °C) [38].

Recommended processing methods for graphene/aluminum composites under different application scenarios and requirements are shown in Table 4 as a reference for industrial manufacturing. While vital for industrial production, liquid-phase methods have clear limits regarding the product properties. Future work should combine SPS with electromagnetic stirring–extrusion to tackle porosity and boost output efficiency simultaneously. It is worth noting that powder metallurgy sintering equipment (such as SPS and HIP) has enabled great technical progress in the past 2–3 years driven by the strong demand for large-format, high-throughput production of dense solid-state batteries electrolytes and electrodes; all the aforementioned sintering technologies are now rapidly evolving toward larger processing dimensions, ultrafast sintering capability, and continuous production mode. The iteration of these equipment has greatly promoted the development of graphene/aluminum alloys.

Among these traditional processing methods, stir casting has a higher level of industrial maturity and is most suitable for mass production. SPS is applicable for high-end, small-batch manufacturing, where superior properties justify the higher processing cost. Remarkable advantages in cost are found in stir casting with about US$1,500 per ton (Table 5). With relatively low equipment investment and mature process routes, large-size

Table 4: The recommended processing methods for graphene/aluminum composites under different application scenarios and requirement.

Application requirement	Recommended process	Advantages	Typical application scenario	Maximum producible component size/weight
ultrahigh strength	SPS (0.3–1.2 wt % GNPs)	grain refinement (0.8 μm), density >99.2%	aero-engine components	400 × 400 × 600 mm, ~200 kg
complex thin-walled structures	semi-solid electromagnetic stirring	equiaxed crystal structure (shape factor 0.84)	new energy vehicle battery casings	10 g to 100 kg
corrosion resistance priority	ARB (0.1–0.5 wt % GO)	corrosion rate reduced by 89%	marine engineering structures	sheets of less than 100mm in width generally
low-cost mass production	stir casting	unit cost below US$25	electronic packaging substrates	diameters of 70–520 mm in generally, same as in direct chill casting

Table 5: Cost breakdown of Gr/Al composites prepared by different routes (excluding the cost of aluminum; benchmarks: 2000 t/a annual production capacity, 0.1–0.5 wt % few-layer graphene loading, unit: US$ per ton, all relevant prices are based on the Chinese market).

Cost item	Stir casting route	SPS route
raw material cost (few-layer graphene)	~900	~900
utility (fuel and power) cost	~88	~60
plant depreciation cost	~100	~300
equipment depreciation cost	~180	~4800
labor cost	~240	~3600
total cost	~1508	~9660

production is easily realized, and excellent compatibility with existing smelting and casting systems of the aluminum industry is achieved. The dispersion of graphene in the melt can be improved to a certain extent by optimizing process parameters such as ball-milled preforms and electromagnetic stirring, and synergistic improvement of strength and plasticity is achieved. This makes stir casting a feasible industrial route for mass, low-cost preparation of Gr/Al composites with moderate performance requirements. Its shortcomings are also obvious: Intense interfacial reactions occur without interface modification of graphene, leading to limited improvement in strength, electrical conductivity, and thermal conductivity of the composites. Consistency control of wire products along the length direction is acceptable, but that of large-section cast products is poor.

Prominent advantages regarding process stability and microstructure control are found in the SPS route. The formation of the harmful interfacial phase Al_4C_3 can be effectively inhibited via the parameters of rapid heating/cooling and pressure-assisted sintering. Although the cost of SPS equipment is relatively high, high process accuracy, strong repeatability, and precise regulation of graphene dispersion and interfacial bonding can be achieved to obtain products with excellent performance. Takt production rather than continuous production is adopted by SPS, so the processing fee is usually above US$9,000 per ton (Table 5) with lower production efficiency, which increases the investment of human resources and equipment. It is especially suitable for scientific research exploration and the production of high-performance, high value-added products, such as high-strength structural components and thermal dissipation materials for AI servers. Besides, it can be seen that the cost of the graphene raw material is not the major expense.

3.2 Advanced novel fabrication strategies

Significant technological advancements in graphene/aluminum composite manufacturing have been observed in recent years. Two methods stand out, namely, additive manufacturing, especially laser powder bed fusion (LPBF), and deformation-driven metallurgical techniques [20,66-70]. LPBF works by melting layers of graphene/aluminum powder with a powerful laser (200–400 W). The powder is melted quickly, and graphene is trapped inside the aluminum as it cools down fast. Finer grains in the metal form due the graphene addition, and the metal is made much stronger by effective load sharing at the interface. To start, the powder mix is made uniform using ball milling or chemical coating, typically adding between 0.1 and 3.0 wt % graphene. The right process parameters are crucial, that is, layer

thickness around 30 μm, laser speed of 800–1200 mm·s^{-1}, and laser path overlap of 20–40%. Careful control is applied to stop graphene from breaking down too much [20,66-70]. Exceptional mechanical enhancement, multifunctional properties, and controlled anisotropy are demonstrated by materials fabricated through this methodology. Tensile strength exhibits a more than 40% improvement relative to pure aluminum, attributable to synergistic dislocation pinning and Orowan strengthening mechanisms [66-68]. While additive manufacturing incurs higher initial capital investment, material waste is substantially reduced to approximately 5% (compared to 20% in conventional casting processes), and total lifecycle costs are consequently diminished [20,66-68].

Deformation-driven metallurgical bonding utilizes intense shear stresses generated during severe plastic deformation (SPD) to exfoliate graphene from graphite precursors in situ. Deformation-induced thermal energy is simultaneously harnessed to establish metallurgical bonding between graphene and the metallic substrate [69,71,72]. In situ graphene exfoliation coupled with dynamic recrystallization of the aluminum matrix was achieved by Huang et al. [73] through high-strain deformation ($\varepsilon > 5$) via friction stir processing (FSP) and associated frictional heating, within a one-minute processing window. A tensile strength of 468 MPa (293.3% enhancement) and exceptional ductility of 19.9% were imparted to the 1.5 wt % GNPs/Al composite [73]. Multipass SPD extrusion (3–7 passes) conducted at 500 °C was employed by Wu et al. [74] to achieve in situ exfoliation of graphite flakes. Shear deformation was exploited to induce interlayer slippage and dissociation of graphite structures, yielding graphene, while dynamic recrystallization was promoted to generate ultrafinely grained microstructure [74]. Similar results were also observed after the processing of our 1% graphite/aluminum composite after severe plastic deformation, as shown in Figure 2.

Graphene/aluminum composite manufacturing technologies are now largely in the early stages of industrialization (Table 6).

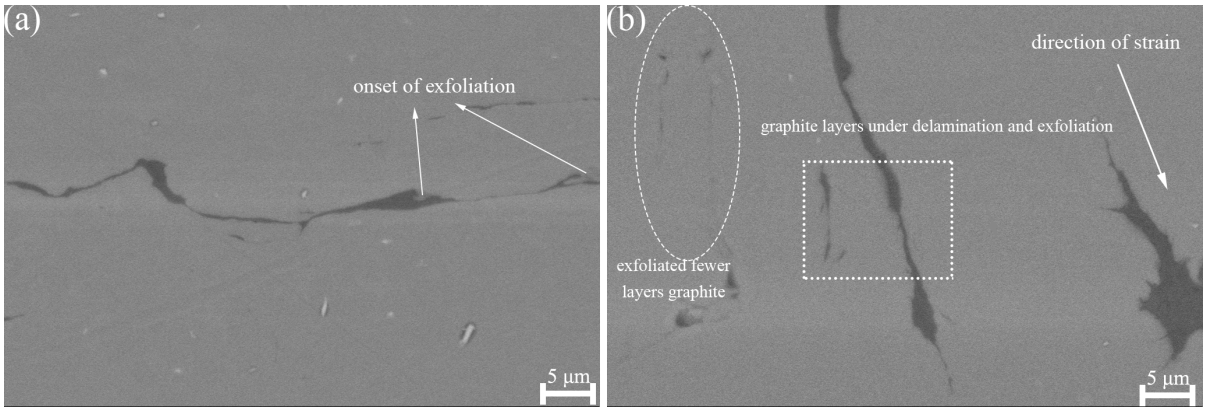


Figure 2: Graphene from graphite in metal matrix composites via severe plastic deformation.

Table 6: Comparison of manufacturing technologies for graphene/aluminum composites.

Manufacturing technology	Technology readiness level	Applicable industrial product types
spark plasma sintering	4–5	high-value precision components, such as aerospace sensors, thermal management devices, and electronic packaging shells
semi-solid electromagnetic stirring	3–4	automotive brake discs, heat sinks, and cost-sensitive castings with relatively simple geometries
stir casting	4–5	low-to-medium-end heat-exchange parts and structural supports, where moderate uniformity can be tolerated
laser powder bed fusion	3–4	customized functional parts with extreme geometric complexity, such as lattice-structured heat sinks and lightweight aerospace brackets
severe plastic deformation (including ARB and FSP)	2–3	high-strength thin sheets, surface strengthening of structural components subjected to harsh local service conditions, such as piston crowns and die surfaces

Low cost and good compatibility with existing infrastructure are offered by liquid-phase routes (stir casting or semi-solid electromagnetic stirring), but dispersion challenges limit their technology readiness levels (TRL), leaving a gap to reliable application. Superior interfacial control is provided by solid-phase routes (SPS or SPD), with SPS reaching the highest TRL of 4–5 and already being suitable for high-value products at a high price. Great promise is held by LPBF, but it remains the least mature technology. The key to industrialization lies in achieving uniform graphene dispersion by interface modification, which is discussed in Section 4, and establishing robust process windows, thereby enabling the transition from laboratory specimens to industrial products.

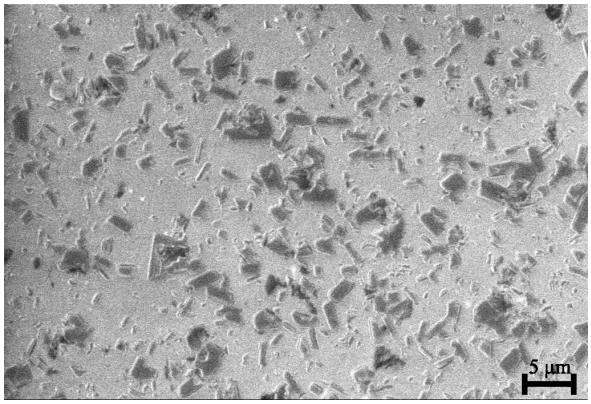


Figure 3: SEM image of Al_4C_3 in a 1% Gr/Al composites sintered at a temperature of 650 °C from our work.

4 Interface engineering and properties change mechanisms

4.1 Interface engineering strategies

The interface between graphene and the aluminum matrix is a defining microstructure that critically influences the overall performance of graphene/aluminum composites. Significant progress in both experimental characterization and computational modeling has been made, and this has deepened the understanding of these interfacial regions and their fundamental behaviors [20,38,45,75-80]. One of the key features at the graphene/aluminum boundary is the formation of the Al_4C_3 phase. The typical microstructure of Al_4C_3 is shown in Figure 3, the morphology is short rod-like/fragmented, protruding after polishing due to high hydrolysis susceptibility. Based on molecular dynamics simulations [75-77], the formation kinetics of Al_4C_3 at graphene/aluminum interfaces is found to follow a diffusion-reaction mechanism. Above 450 °C, aluminum atoms are observed to diffuse through graphene edge defects to form tetrahedrally arranged Al–C bonds, and the reaction kinetics is dominated by three factors. Within the temperature range of 550–630 °C, the rate constant is found to adhere to an Arrhenius relationship with an activation energy barrier of 156 kJ·mol^{-1} for atomic migration and bond reorganization. The crystallographic orientation was shown to significantly modulate reactivity, the prismatic facets exhibit 40% higher activity than the basal (0001) planes due to abundant step edges and dangling bonds, whereas the dense atomic arrangement of the planes imposes greater kinetic resistance. Defect engineering was found to play a catalytic role; single vacancies reduce the reaction energy barrier by 0.8 eV (~77.2 kJ·mol^{-1}) by releasing local strain and exposing highly reactive carbon atoms [78]. These atomic-scale insights enable precise control of interfacial Al_4C_3 growth through synergistic optimization of temperature, defect density, and graphene orientation.

It is crucial to note that excessive Al_4C_3 formation is detrimental and leads to interfacial brittleness and heightened susceptibility to degradation by moisture [20,38]. However, the precise functional role of Al_4C_3 remains a topic of active debate. To probe the atomic-scale formation dynamics of Al_4C_3, a neural evolutionary potential (NEP) model was developed by researchers [81]. Simulations based on this model suggest that controlled formation of Al_4C_3 at the interface can be beneficial. It appears to strengthen interfacial bonding by creating a network of robust covalent bonds. Molecular dynamics simulations leveraging the NEP potential revealed that composites with such Al_4C_3-modified interfaces exhibit impressive mechanical properties. Under tensile loading parallel to the interface, ultimate strengths greater than 2 GPa were achieved [81]. This represents a substantial increase compared to pure aluminum. Analysis of shear deformation further showed that the covalent interfacial bonds significantly raise the energy barrier for atomic slip approximately threefold. Consequently, these composites are observed to combine exceptional strength with retained ductility levels of 15–25%, and this balance is often difficult to achieve.

The key factor determining the influence of Al_4C_3 is its quantity at the interface. When the processing temperature is controlled within the range of 450–630 °C, and the holding time is kept short, very little Al_4C_3 forms in the form of discontinuous nanoscale particles at the interface. In this case, the beneficial effects are dominant. It has been shown by studies that the interfacial reaction rate between graphene and aluminum is very slow below 600 °C, and only small quantities of fine Al_4C_3 are yielded. These fine Al_4C_3 nanoparticles can serve as chemical anchoring points at the interface, and the originally weak physical bonding is transformed into locally strong chemical bonding. Thereby, the load transfer efficiency is enhanced. Therefore, under low-temperature solid-state processing or short-duration rapid sintering conditions, the thermal input is insuffi-

cient to drive excessive Al_4C_3 reaction. The interfacial reaction products are limited, and the beneficial effects dominate the material properties. When the processing temperature exceeds the melting point of aluminum (660 °C) or prolonged high-temperature holding is applied, the two-dimensional structure of graphene suffers severe damage. The reaction rate between graphene and aluminum is increased significantly, and this leads to rapid and massive formation of Al_4C_3. At this point, the detrimental effects sharply take the dominant role. Table 7 shows the comparison of different graphene/aluminum composite processing methods from the perspective of Al_4C_3 formation.

To decrease the harmful interfacial reactions, multiple interfacial modifications have been suggested by researchers. In direct Al/graphene reactive interfaces, strategic modulation of sintering temperature and dwell time facilitates controlled formation of nanoscale Al_4C_3 at the Al/graphene interface, and robust covalent bonding networks are established. It has been established by research that the $(001)Al \parallel (0001)Al_4C_3$ orientation relationship yields optimal mechanical properties [21,81,82]. Intermediate-phase modified interfaces incorporate Al_2O_3 or Al_4SiC_4 as transition layers, and this enables controlled load transfer while interfacial bonding strength is enhanced and deleterious interfacial reactions are suppressed [82]. Besides, coating metals on graphene layers are considered an effective method to solve the poor interface bonding [82]. Ni is the best coating metal, enhancing interfacial strength by 145.34% due to the highest value of pullout force. Additionally, three-dimensional topological interfaces have been developed. Inspired by origami principles, graphene origami (GOri) structures were designed by researchers [83]. Uniform stress distribution along crease edges is ensured through this configuration by specific unfolding behavior. The distinctive folded topology of GOri has demonstrated a 37% enhancement in indentation load with a 138% increase in indentation depth, and stress concentration phenomena inherent to conventional two-dimensional graphene architectures are effectively mitigated.

4.2 Property-change mechanisms

It has been confirmed by researches that graphene addition significantly improves the strength and hardness of aluminum matrix composites [17,20,22,38]. Innovative interface design further allows for simultaneous improvement of both strength and ductility. The strengthening mechanisms in graphene/aluminum composites include not only those seen in common aluminum alloys, such as fine-grain strengthening, dislocation strengthening, particle strengthening, and solid solution strengthening, but also effects unique to graphene itself. These specific mechanisms from graphene involve load transfer strengthening, grain refinement induced by graphene, Orowan strengthening mediated by graphene, and strain hardening by graphene [17,20,22,38].

Shear lag theory says that when the interfacial bonding strength reaches a critical level, external loads are effectively transferred to graphene reinforcements through interfacial shear stress. This explains the load transfer [45,48,51]. These findings are supported by experimental studies on GNP/Al composites made by ball milling and semi-solid stirring. Adding GNPs increased composite hardness by ~40% and tensile strength by ~35%. This improvement comes from combined effects of GNP load transfer strengthening and grain refinement [48,51]. Graphene is also found to act as a nucleation site for aluminum crystallization while grain boundary movement is blocked during processing [38,84]. This causes significant grain refinement. In AA-3003/GNPs and AA-5154/GNPs composites, fast solidification, and non-equilibrium nucleation shrank grains to sub-micrometer sizes [85]. Besides, dislocation motion is blocked by graphene, and dislocations accumulate at the interfaces. Higher stress is needed for dislocations to bypass or cut through reinforcements, and this leads to Orowan strengthening and higher yield strength [86]. Then, during plastic deformation, an increase in the geometrically necessary dislocation density at the interface is induced by graphene, and this results in an additional 54 MPa of flow stress at a 5.8% strain in 0.50 vol % graphene nanosheet/Al [87].

Table 7: Interfacial reactions in main synthesis methods of graphene/aluminum composites.

Method	Temperature range (°C)	Graphene content (vol %)	Interfacial reactions	Typical performance enhancement
ball milling + hot pressing	400–600	0.5–5.0	prone to Al_4C_3 formation	47% increase in hardness [44]
melt ultrasonic dispersion	660–800	0.1–2.0	high amounts of Al_4C_3, requires barrier coating	75% increase in thermal conductivity [39]
multipass friction stir processing	400–500	1.0–3.0	no Al_4C_3 formation	threefold increase in yield strength [38]
vacuum-assisted infiltration	700–900	3.0–10.0	high amounts of Al_4C_3, requires preform	230% increase in flexural strength [20]

Electrical and thermal conductivities of graphene/aluminum composites are critically governed by graphene dispersion homogeneity and interfacial properties [34,45,88-90]. According to calculations, the electrical conductivity of Al composites generally increases with graphene adding, and this is attributed to percolating conductive network formation [34]. However, the measured interfacial resistivity is around 10^{-8} Ω·m, and this substantially suppresses theoretical performance gains [34]. After vacuum hot-press sintering of a 0.5 wt % graphene/aluminum composite, graphene was uniformly dispersed at the grain boundaries in the Al matrix. The resulting composite had thermal and electrical conductivities higher by 7.1% and 4.0%, respectively, compared to pure Al [88]. A conductivity test on multilayer graphene/aluminum obtained through high-pressure torsion (HPT) was conducted by Huang and coworkers [90]. The results showed that when 5% graphene is used, the conductivity is significantly increased to 64.9–66.7% IACS, and this surpasses the theoretical conductivity of pure high-purity aluminum. This is attributed to the uniform and linear arrangement of graphene (Figure 4).

Regarding thermal conduction, the interfacial phonon transport mechanism serves as the core factor determining the overall performance of such composites [91-94]. It has been demonstrated that despite the ultrahigh intrinsic thermal conductivity of graphene, composites fabricated by incorporating graphene into matrices of metals often fail to achieve the expected improvement in thermal conductivity, and even a reduction in this property is exhibited. The fundamental bottleneck underlying this counterintuitive phenomenon is the high interfacial thermal resistance (ITR). ITR mainly originates from two effects, namely phonon spectrum mismatch and phonon localization. The former refers to the mismatch in phonon vibration frequencies between metals and graphene, while the latter describes the phenomenon where phonons are confined near the interface. Interfacial bonding characteristics are found to exert a decisive influence on the ITR. In addition, the density and phonon spectrum characteristics of the metal matrix, graphene strain induced by lattice mismatch, and various defects in the interfacial region are found to exert synergistic regulatory effects on phonon transport efficiency. Accordingly, strengthening interfacial phonon coupling is recognized as the key pathway to improve the thermal conductivity of such composites. This conclusion not only provides theoretical guidance for design strategies of high-performance thermal management materials by interfacial alloying, but also lays a theoretical foundation for retarding thermal conduction via structural regulation including constructing disordered interfaces, so that novel thermal insulation materials and thermoelectric materials can be developed.

Employing density functional theory (DFT) and the non-equilibrium Green's function formalism, phonon transport characteristics and interfacial heat transfer efficiency at metal-encapsulated graphene heterostructures were examined by Tao et al. [95-97] and Chen and coworkers [98,99]. The systems

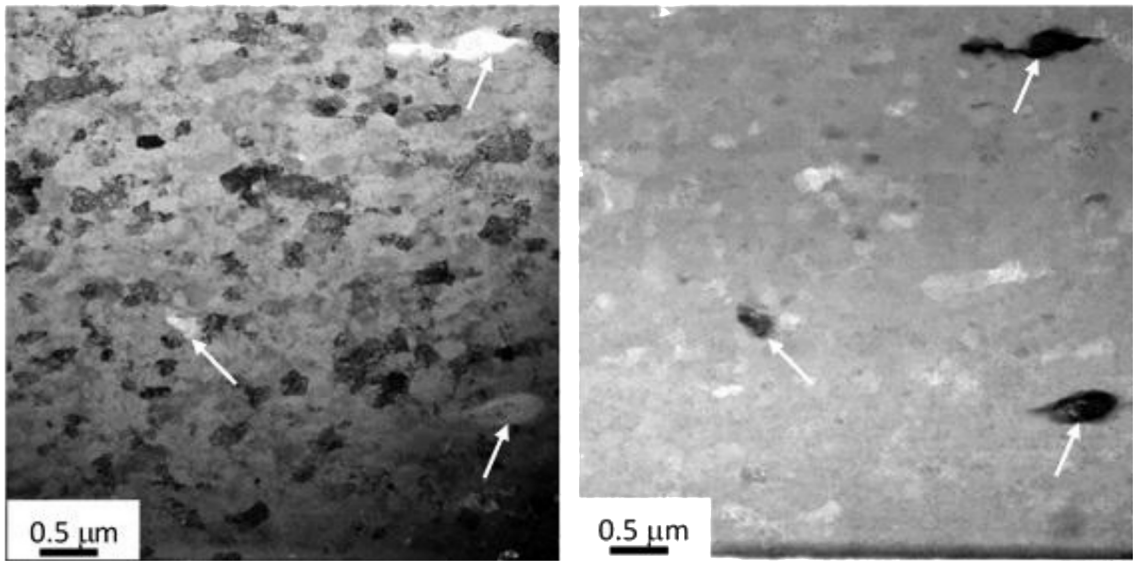


Figure 4: STEM and Z-contrast images showing the microstructures of GNP/Al uniform and linear arrangement processed by HPT at 473 K for N = 20 rotations (Reproduced from [90] (© 2018 Y. Huang, et al., published by Elsevier Ltd on behalf of Acta Materialia Inc., distributed under the terms of the Creative Commons Attribution-NonCommercial-NoDerivatives 4.0 International License, http://creativecommons.org/licenses/by-nc-nd/4.0/. This content is not subject to CC BY 4.0).

comprised monolayer graphene, double-sided hydrogenated graphene, and single-sided hydrogenated graphene sandwiched between copper and nickel substrates. Their computational results reveal a critical dependency of thermal conductance across metal/Gr/metal interfaces on the nature of graphene–metal bonding. Specifically, chemical bonding (chemisorption) is found to significantly boost interfacial thermal conductance, whereas physical adsorption mechanisms markedly suppress it. To experimentally validate this phenomenon, a novel methodology for enhancing thermal transport at metal–graphite junctions was developed by them. After focused ion beam (FIB) milling pretreatment of graphite substrates, the interfacial thermal conductance between aluminum and graphite was fivefold enhanced [97]. This substantial improvement correlates with the reduction in Fermi level energy observed in milled graphite relative to untreated specimens. The modified electronic structure facilitates stronger interfacial coupling, and phonon-mediated heat transfer across the hybrid interface is thereby optimized. This provides a new feasible approach for further leveraging the conductive and thermal properties of graphene and developing high-performance graphene/aluminum alloys.

5 Conclusion, future applications and challenges

Graphene/aluminum composites exhibit exceptional mechanical, thermal, and electrical properties, and they are positioned as transformative materials for high-performance industrial applications. How to produce materials with high performance at a low cost is regarded as the most significant issue from the perspective of industrialization. The industrialization of high-performance Gr/Al composites is currently hindered by the C–Al interface, which is inherently unstable and difficult to regulate. Excessive detrimental interfacial reactions severely impair the strength of the composites; also, they act as a critical barrier to phonon transport. The energy interfacial resistance is pushed to an unacceptably high level. The connection between graphene and aluminum is usually only maintained by weak van der Waals forces, and such adsorption force is insufficient to realize effective load transfer or energy conduction. This is the root of the issue of interfacial bonding.

The most feasible solution is low-cost surface modification of graphene. Instead of directly mixing pristine graphene with aluminum, the graphene surface is coated or modified with a thin and uniform transition layer. This coating must protect the carbon material from erosion by aluminum melt and inhibit the formation of Al_4C_3. Besides, it must convert the interface from a region dominated by weak physical adsorption to one with strong chemical bonding. Elements including Cu, Ti, or Ni, deposited on the graphene surface via scalable chemical or electrochemical routes, can form stable thin-layer carbides or intermetallic compounds that act as robust bridges between the two components. This engineered layer can significantly improve phonon coupling and reduce interfacial resistance of energy transfer.

Suitable methods need to be developed to cut the cost of composite processing while performance is maintained. If the carefully constructed interface is damaged during the subsequent consolidation and forming process, even the most sophisticated surface modification will be rendered futile. Conventional powder metallurgy routes involve long-term high-temperature sintering, and this may lead to decomposition or coarsening of the protective coating. Casting is low in cost, but it faces inherent challenges in wetting, dispersion, and uniformity control. Processing innovations that operate at lower temperatures and shorter holding times are required by the industry, such as combining advanced solid-phase processes like SPS with low-cost solutions like stir casting. Because of the requirements regarding solid-state batteries and the thermal management of artificial intelligence chips, the capacity of SPS and other isopressing equipment has been significantly enhanced. These routes can complete composite consolidation rapidly, the fragile interfacial structure is preserved, and uniform dispersion rather than agglomeration of the modified graphene is ensured.

Future research efforts should be prioritized as follows: (1) low-cost protective coatings on graphene to enhance interfacial adhesion through covalent bonding mechanisms, alloy coating, vacancy engineering, hydrogenation, and FIB treatments and (2) rapid low-temperature consolidation methods such as rapid spark plasma sintering combined with casting.

Funding

Thanks to the China Postdoctoral Foundation for supporting this article.

Author Contributions

Shuai GuoLiang: conceptualization; data curation; funding acquisition; investigation; methodology; project administration; resources; supervision; writing – review & editing. Pan LinXia: data curation; methodology; writing – original draft. Ma HaiLin: conceptualization; supervision; writing – review & editing.

ORCID® iDs

Shuai GuoLiang - https://orcid.org/0000-0002-8254-3062

Data Availability Statement

All data that supports the findings of this study is available in the published article and/or the supporting information of this article.

References

1. Hsieh, C.-T.; Ho, Y.-C.; Wang, H.; Sugiyama, S.; Yanagimoto, J. *Mater. Sci. Eng., A* **2020,** *786,* 138998. doi:10.1016/j.msea.2020.138998
2. Li, Z.; Fan, G.; Guo, Q.; Li, Z.; Su, Y.; Zhang, D. *Carbon* **2015,** *95,* 419–427. doi:10.1016/j.carbon.2015.08.014
3. Yi, M.; Shen, Z. *J. Mater. Chem. A* **2015,** *3,* 11700–11715. doi:10.1039/c5ta00252d
4. Lee, W.; Jang, S.; Kim, M. J.; Myoung, J.-M. *Nanotechnology* **2008,** *19,* 285701. doi:10.1088/0957-4484/19/28/285701
5. Bartolucci, S. F.; Paras, J.; Reif, J.; Rafiee, J.; Lee, S.; Kapoor, D.; Koratkar, N. *Mater. Sci. Eng., A* **2011,** *528,* 7933–7937. doi:10.1016/j.msea.2011.07.043
6. Pérez-Bustamante, R.; Bolaños-Morales, D.; Bonilla-Martínez, J.; Estrada-Guel, I.; Martínez-Sánchez, R. *J. Alloys Compd.* **2014,** *615,* S578–S582. doi:10.1016/j.jallcom.2014.01.225
7. Lee, C.; Wei, X.; Kysar, J. W.; Hone, J. *Science* **2008,** *321,* 385–388. doi:10.1126/science.1157996
8. Balandin, A. A.; Ghosh, S.; Bao, W.; Calizo, I.; Teweldebrhan, D.; Miao, F.; Lau, C. N. *Nano Lett.* **2008,** *8,* 902–907. doi:10.1021/nl0731872
9. Novoselov, K. S.; Geim, A. K.; Morozov, S. V.; Jiang, D.; Zhang, Y.; Dubonos, S. V.; Grigorieva, I. V.; Firsov, A. A. *Science* **2004,** *306,* 666–669. doi:10.1126/science.1102896
10. Stoller, M. D.; Park, S.; Zhu, Y.; An, J.; Ruoff, R. S. *Nano Lett.* **2008,** *8,* 3498–3502. doi:10.1021/nl802558y
11. Zhu, P.-j.; Yan, Y.-n.; Zhou, Y.; Qi, Z.-j.; Li, Y.-f.; Chen, C.-M. *ACS Appl. Nano Mater.* **2024,** *7,* 8445–8463. doi:10.1021/acsanm.4c00411
12. Sang, M.; Shin, J.; Kim, K.; Yu, K. J. *Nanomaterials* **2019,** *9,* 374. doi:10.3390/nano9030374
13. Fu, S.; Zhou, Y.; Xu, K.; Huang, G.; Wang, Z.; Ni, Y.; Huang, X.; Zhang, C.; Wang, Y. *Nanoscale* **2026,** *18,* 6687–6712. doi:10.1039/d5nr05318h
14. Chen, W.; Yang, T.; Dong, L.; Elmasry, A.; Song, J.; Deng, N.; Elmarakbi, A.; Liu, T.; Lv, H. B.; Fu, Y. Q. *Nanotechnol. Precis. Eng.* **2020,** *3,* 189–210. doi:10.1016/j.npe.2020.12.003
15. Khanna, V.; Kumar, V.; Bansal, S. A.; Prakash, C.; Ubaidullah, M.; Shaikh, S. F.; Pramanik, A.; Basak, A.; Shankar, S. *J. Mater. Res. Technol.* **2023,** *22,* 3402–3412. doi:10.1016/j.jmrt.2022.12.161
16. Zhang, J.; Qian, M.; Zhang, X.; Li, A.; Geng, L. *Mater. Des.* **2024,** *244,* 113099. doi:10.1016/j.matdes.2024.113099
17. Md Ali, A.; Omar, M. Z.; Hashim, H.; Salleh, M. S.; Mohamed, I. F. *Rev. Adv. Mater. Sci.* **2021,** *60,* 801–817. doi:10.1515/rams-2021-0062
18. Cao, J.; Li, F.; Yang, Q.; Zhan, K.; Yang, Z.; Wang, Z.; Zhao, B. *Compos. Interfaces* **2023,** *30,* 543–583. doi:10.1080/09276440.2023.2179248
19. Ranjan, R.; Bajpai, V. *J. Compos. Mater.* **2021,** *55,* 2369–2413. doi:10.1177/0021998320988566
20. Su, J.; Teng, J. *Front. Mater. Sci.* **2021,** *15,* 79–97. doi:10.1007/s11706-021-0541-0
21. Mourdjeva, Y.; Karashanova, D.; Nihtianova, D.; Lazarova, R. *J. Mater. Eng. Perform.* **2024,** *33,* 11607–11616. doi:10.1007/s11665-023-08804-6
22. Alam, M. A.; Ya, H. B.; Azeem, M.; Mustapha, M.; Yusuf, M.; Masood, F.; Marode, R. V.; Sapuan, S. M.; Ansari, A. H. *Nanotechnol. Rev.* **2023,** *12,* 20230111. doi:10.1515/ntrev-2023-0111
23. Zhao, Z. Y.; Zhao, W. J.; Bai, P. K.; Wu, L. Y.; Huo, P. C. *Mater. Lett.* **2019,** *255,* 126559. doi:10.1016/j.matlet.2019.126559
24. Xiong, B.; Liu, K.; Xiong, W.; Wu, X.; Sun, J. *J. Alloys Compd.* **2020,** *845,* 156282. doi:10.1016/j.jallcom.2020.156282
25. Shin, S. E.; Choi, H. J.; Shin, J. H.; Bae, D. H. *Carbon* **2015,** *82,* 143–151. doi:10.1016/j.carbon.2014.10.044
26. Gao, X.; Yue, H.; Guo, E.; Zhang, H.; Lin, X.; Yao, L.; Wang, B. *Mater. Des.* **2016,** *94,* 54–60. doi:10.1016/j.matdes.2016.01.034
27. Seyed Pourmand, N.; Asgharzadeh, H. *Crit. Rev. Solid State Mater. Sci.* **2020,** *45,* 289–337. doi:10.1080/10408436.2019.1632792
28. Geim, A. K.; Novoselov, K. S. *Nat. Mater.* **2007,** *6,* 183–191. doi:10.1038/nmat1849
29. Eigler, S.; Hirsch, A. *Angew. Chem., Int. Ed.* **2014,** *53,* 7720–7738. doi:10.1002/anie.201402780
30. Georgakilas, V.; Otyepka, M.; Bourlinos, A. B.; Chandra, V.; Kim, N.; Kemp, K. C.; Hobza, P.; Zboril, R.; Kim, K. S. *Chem. Rev.* **2012,** *112,* 6156–6214. doi:10.1021/cr3000412
31. Li, X.; Wang, X.; Zhang, L.; Lee, S.; Dai, H. *Science* **2008,** *319,* 1229–1232. doi:10.1126/science.1150878
32. Balkanloo, P. G.; Sharifi, K. M.; Marjani, A. P. *Mater. Adv.* **2023,** *4,* 4272–4293. doi:10.1039/d3ma00372h
33. Zhao, W.; Fang, M.; Wu, F.; Wu, H.; Wang, L.; Chen, G. *J. Mater. Chem.* **2010,** *20,* 5817–5819. doi:10.1039/c0jm01354d
34. Khanna, V.; Singh, K.; Kumar, S.; Bansal, S. A.; Channegowda, M.; Kong, I.; Khalid, M.; Chaudhary, V. *ECS J. Solid State Sci. Technol.* **2022,** *11,* 127001. doi:10.1149/2162-8777/aca933
35. Berger, C.; Song, Z.; Li, X.; Wu, X.; Brown, N.; Naud, C.; Mayou, D.; Li, T.; Hass, J.; Marchenkov, A. N.; Conrad, E. H.; First, P. N.; de Heer, W. A. *Science* **2006,** *312,* 1191–1196. doi:10.1126/science.1125925
36. Marcano, D. C.; Kosynkin, D. V.; Berlin, J. M.; Sinitskii, A.; Sun, Z.; Slesarev, A.; Alemany, L. B.; Lu, W.; Tour, J. M. *ACS Nano* **2010,** *4,* 4806–4814. doi:10.1021/nn1006368
37. Parviz, D.; Irin, F.; Shah, S. A.; Das, S.; Sweeney, C. B.; Green, M. J. *Adv. Mater. (Weinheim, Ger.)* **2016,** *28,* 8796–8818. doi:10.1002/adma.201601889
38. Kumar, P. L.; Lombardi, A.; Byczynski, G.; Murty, S. N.; Murty, B. S.; Bichler, L. *Prog. Mater. Sci.* **2022,** *128,* 100948. doi:10.1016/j.pmatsci.2022.100948
39. Zhang, C.; Li, H.; Chen, S.; Jiao, L.; Shen, W.; Song, Z.; Wang, J.; Nie, Z.; Shcheretskyi, O. *Mater. Today Commun.* **2025,** *48,* 113606. doi:10.1016/j.mtcomm.2025.113606
40. Bonaccorso, F.; Lombardo, A.; Hasan, T.; Sun, Z.; Colombo, L.; Ferrari, A. C. *Mater. Today* **2012,** *15,* 564–589. doi:10.1016/s1369-7021(13)70014-2
41. Adetayo, A.; Runsewe, D. *Open J. Compos. Mater.* **2019,** *9,* 207–229. doi:10.4236/ojcm.2019.92012
42. Razaq, A.; Bibi, F.; Zheng, X.; Papadakis, R.; Jafri, S. H. M.; Li, H. *Materials* **2022,** *15,* 1012. doi:10.3390/ma15031012
43. Jia, X.; Campos-Delgado, J.; Terrones, M.; Meunier, V.; Dresselhaus, M. S. *Nanoscale* **2011,** *3,* 86–95. doi:10.1039/c0nr00600a
44. Zhou, T.; Lei, M.; Xu, J. *Mater. Today Sustainability* **2024,** *25,* 100674. doi:10.1016/j.mtsust.2024.100674
45. Wang, J.; Li, Z.; Fan, G.; Pan, H.; Chen, Z.; Zhang, D. *Scr. Mater.* **2012,** *66,* 594–597. doi:10.1016/j.scriptamat.2012.01.012
46. Han, T.; Li, J.; Zhao, N.; He, C. *Carbon* **2020,** *159,* 311–323. doi:10.1016/j.carbon.2019.12.029

47. Yang, Z.; Ni, Z.; Yan, J.; Fan, L.; Zhang, J.; Chen, X.; Guan, R. *Carbon* **2025,** *238,* 120213. doi:10.1016/j.carbon.2025.120213
48. Bhadauria, A.; Singh, L. K.; Laha, T. *Mater. Sci. Eng., A* **2019,** *749,* 14–26. doi:10.1016/j.msea.2019.02.007
49. Bastwros, M.; Kim, G.-Y.; Zhu, C.; Zhang, K.; Wang, S.; Tang, X.; Wang, X. *Composites, Part B* **2014,** *60,* 111–118. doi:10.1016/j.compositesb.2013.12.043
50. Gürbüz, M.; Can Şenel, M.; Koç, E. *J. Compos. Mater.* **2018,** *52,* 553–563. doi:10.1177/0021998317740200
51. Bisht, A.; Srivastava, M.; Kumar, R. M.; Lahiri, I.; Lahiri, D. *Mater. Sci. Eng., A* **2017,** *695,* 20–28. doi:10.1016/j.msea.2017.04.009
52. Tian, W.-m.; Li, S.-m.; Wang, B.; Chen, X.; Liu, J.-h.; Yu, M. *Int. J. Miner., Metall. Mater.* **2016,** *23,* 723–729. doi:10.1007/s12613-016-1286-0
53. Khoshghadam-Pireyousefan, M.; Rahmanifard, R.; Orovcik, L.; Švec, P.; Klemm, V. *Mater. Sci. Eng., A* **2020,** *772,* 138820. doi:10.1016/j.msea.2019.138820
54. Tokita, M. *Ceramics (Basel, Switz.)* **2021,** *4,* 160–198. doi:10.3390/ceramics4020014
55. Singh, V. P.; Gupta, G. K.; Mishra, S. *J. Mater. Eng. Perform.* **2025,** *35,* 8917–8933. doi:10.1007/s11665-025-12275-2
56. Huang, C.-y.; Hu, S.-p.; Chen, K. *Int. J. Miner., Metall. Mater.* **2019,** *26,* 752–759. doi:10.1007/s12613-019-1780-2
57. Tiwari, J. K.; Mandal, A.; Rudra, A.; Mukherjee, D.; Sathish, N. *J. Alloys Compd.* **2019,** *801,* 49–59. doi:10.1016/j.jallcom.2019.06.127
58. Mortazavi, S. S.; Sangpour, P.; Rahmanifard, R. *J. Compos. Mater.* **2026,** *60,* 965–980. doi:10.1177/00219983251371616
59. Wang, J.; Chen, J.; Du, S.; Wu, R.; Cao, Y.; Feng, Y. *J. Mater. Res. Technol.* **2026,** *40,* 427–439. doi:10.1016/j.jmrt.2025.12.119
60. Sharma, S. K.; Gajević, S.; Sharma, L. K.; Pradhan, R.; Sharma, Y.; Miletić, I.; Stojanović, B. *Lubricants* **2024,** *12,* 421. doi:10.3390/lubricants12120421
61. Ali, A. M.; Omar, M. Z.; Salleh, M. S.; Mohamed, I. F.; Anuar, N. F. B. W. *Mater. Sci. Forum* **2023,** *1101,* 3–8. doi:10.4028/p-4brbcm
62. Andilab, B.; Emadi, P.; Ravindran, C. *Materials* **2022,** *15,* 7232. doi:10.3390/ma15207232
63. Lin, G. E. N. G.; Zhang, H. W.; Huang, L. J. *Trans. Nonferrous Met. Soc. China* **2011,** *21,* s274–s279. doi:10.1016/s1003-6326(11)61590-2
64. Boostani, A. F.; Yazdani, S.; Khosroshahi, R. A.; Jiang, Z. Y.; Wei, D. *Mater. Sci. Eng., A* **2018,** *736,* 316–322. doi:10.1016/j.msea.2018.09.001
65. Siddiqui, V. U.; Sapuan, S. M.; Hassan, M. R. *Def. Technol.* **2025,** *43,* 13–25. doi:10.1016/j.dt.2024.04.018
66. Tiwari, J. K.; Mandal, A.; Sathish, N.; Agrawal, A. K.; Srivastava, A. K. *Addit. Manuf.* **2020,** *33,* 101095. doi:10.1016/j.addma.2020.101095
67. Tiwari, J. K.; Mandal, A.; Sathish, N.; Kumar, S.; Ashiq, M.; Nagini, M.; Sharma, R. K.; Agrawal, A. K.; Rajput, P.; Srivastava, A. K. *J. Alloys Compd.* **2022,** *890,* 161725. doi:10.1016/j.jallcom.2021.161725
68. Chen, B.; Xi, X.; Tan, C.; Song, X. *Curr. Opin. Chem. Eng.* **2020,** *28,* 28–35. doi:10.1016/j.coche.2020.01.005
69. Tiwari, J. K.; Mandal, A.; Rudra, A.; Sathish, N.; Kumar, S.; Singh, A. K. *Mater. Chem. Phys.* **2020,** *248,* 122939. doi:10.1016/j.matchemphys.2020.122939
70. Lopez, J. J.; Williams, M. B.; Rushing, T. W.; Confer, M. P.; Ghosh, A.; Griggs, C. S.; Jordon, J. B.; Thompson, G. B.; Allison, P. G. *Materialia* **2022,** *23,* 101440. doi:10.1016/j.mtla.2022.101440
71. Xie, Y.; Meng, X.; Chang, Y.; Mao, D.; Yang, Y.; Xu, Y.; Wan, L.; Huang, Y. *Compos. Sci. Technol.* **2022,** *219,* 109225. doi:10.1016/j.compscitech.2021.109225
72. Mei, Y.; Shao, P.-z.; Sun, M.; Chen, G.-q.; Hussain, M.; Huang, F.-l.; Zhang, Q.; Gao, X.-s.; Pei, Y.-y.; Zhong, S.-j.; Wu, G.-h. *Int. J. Miner., Metall. Mater.* **2020,** *27,* 888–899. doi:10.1007/s12613-020-2048-6
73. Huang, Y.; Xie, Y.; Meng, X. Graphene Nanoplatelet-Reinforced Aluminum Matrix Composites. *Friction Stir Welding and Processing. Materials Forming, Machining and Tribology;* Springer: Singapore, 2024; pp 337–384. doi:10.1007/978-981-99-8688-0_9
74. Wu, G.; Yu, Z.; Jiang, L.; Zhou, C.; Deng, G.; Deng, X.; Xiao, Y. *Carbon* **2019,** *152,* 932–945. doi:10.1016/j.carbon.2019.06.077
75. Yan, Y.-F.; Kou, S.-Q.; Yang, H.-Y.; Dong, B.-X.; Shu, S.-L.; Chen, L.-Y.; Qiu, F.; Zhang, L.-C. *J. Mater. Process. Technol.* **2023,** *317,* 117995. doi:10.1016/j.jmatprotec.2023.117995
76. Huang, J.; Liu, Y.; Lai, Z.; Hu, J.; Zhou, F.; Zhu, J. *Vacuum* **2022,** *204,* 111346. doi:10.1016/j.vacuum.2022.111346
77. Huang, J.; Li, M.; Chen, J.; Cheng, Y.; Lai, Z.; Hu, J.; Zhou, F.; Qu, N.; Liu, Y.; Zhu, J. *Surf. Interfaces* **2023,** *38,* 102825. doi:10.1016/j.surfin.2023.102825
78. Wang, X.; Zhao, J.; Cui, E.; Tian, X.; Sun, Z. *Nanomaterials* **2021,** *11,* 1374. doi:10.3390/nano11061374
79. Wang, W.; Cui, C.; Xia, F.; Xu, W.; Gang, T.; Chen, L. *Sci. Rep.* **2025,** *15,* 38571. doi:10.1038/s41598-025-22443-y
80. Luo, Y.; Huang, Y.; Wang, W.; Yu, S.; Quanfang, C. *Surf. Interfaces* **2024,** *46,* 104164. doi:10.1016/j.surfin.2024.104164
81. Wu, Y.-C.; Chang, X.; Yu, Z. G.; Zhang, Y.-W.; Shao, J.-L. *Mech. Mater.* **2025,** *209,* 105428. doi:10.1016/j.mechmat.2025.105428
82. Wang, X.; Xiao, W.; Wang, J.; Sun, L.; Shi, J.; Guo, H.; Liu, Y.; Wang, L. *Adv. Powder Technol.* **2021,** *32,* 2585–2590. doi:10.1016/j.apt.2021.05.041
83. Wang, Y.; Zhang, Y.; Zhao, S.; Dong, B.; Yang, J.; Zhang, Y. *Compos. Struct.* **2026,** *377,* 119898. doi:10.1016/j.compstruct.2025.119898
84. Zhang, B.; Wang, X.; Liu, C.; Li, X. *AIMS Mater. Sci.* **2018,** *5,* 338. doi:10.3934/matersci.2018.2.338
85. Brodova, I.; Yolshina, L.; Razorenov, S.; Rasposienko, D.; Petrova, A.; Shirinkina, I.; Shorokhov, E.; Muradymov, R.; Garkushin, G.; Savinykh, A. *Metals (Basel, Switz.)* **2022,** *12,* 1054. doi:10.3390/met12061054
86. Venkatraman, M.; Xavior, M. A. *Results Eng.* **2025,** *25,* 104492. doi:10.1016/j.rineng.2025.104492
87. Jiang, Y.; Xu, R.; Tan, Z.; Ji, G.; Fan, G.; Li, Z.; Xiong, D.-B.; Guo, Q.; Li, Z.; Zhang, D. *Carbon* **2019,** *146,* 17–27. doi:10.1016/j.carbon.2019.01.094
88. Zhou, W.; Mikulova, P.; Fan, Y.; Kikuchi, K.; Nomura, N.; Kawasaki, A. *Composites, Part B* **2019,** *167,* 93–99. doi:10.1016/j.compositesb.2018.12.018
89. Wang, J.; Guo, L.-n.; Lin, W.-m.; Chen, J.; Liu, C.-l.; Chen, S.-d.; Zhang, S.; Zhen, T.-t. *New Carbon Mater.* **2019,** *34,* 275–285. doi:10.1016/s1872-5805(19)60016-8
90. Huang, Y.; Bazarnik, P.; Wan, D.; Luo, D.; Pereira, P. H. R.; Lewandowska, M.; Yao, J.; Hayden, B. E.; Langdon, T. G. *Acta Mater.* **2019,** *164,* 499–511. doi:10.1016/j.actamat.2018.10.060
91. Wang, X.; Wang, X.; Wang, Z.; Guo, Y.; Wang, Y. *Mater. Today Commun.* **2020,** *25,* 101431. doi:10.1016/j.mtcomm.2020.101431
92. Yang, H.; Tang, Y.; Yang, P. *Nanoscale* **2019,** *11,* 14155–14163. doi:10.1039/c9nr03538a

93. Sainudeen, S. S.; Joseph, A.; Joseph, M.; Sajith, V. *Appl. Therm. Eng.* **2022,** *212,* 118545. doi:10.1016/j.applthermaleng.2022.118545
94. Shen, Y.; Tang, Y.; Fu, J.; Li, D.; Yang, B.; Cai, Y.; Liu, Z. *Int. Commun. Heat Mass Transfer* **2026,** *172,* 110320. doi:10.1016/j.icheatmasstransfer.2025.110320
95. Tao, Y.; Wu, C.; Qi, H.; Liu, C.; Wu, X.; Hao, M.; Wei, Z.; Yang, J.; Chen, Y. *Nanoscale* **2020,** *12,* 14838–14846. doi:10.1039/c9nr09937a
96. Tao, Y.; Liu, C.; Chen, W.; Cai, S.; Chen, C.; Wei, Z.; Bi, K.; Yang, J.; Chen, Y. *Phys. Lett. A* **2017,** *381,* 1899–1904. doi:10.1016/j.physleta.2017.03.020
97. Zhao, Y.; Tao, Y.; Xu, W.; Huang, S.; Guo, M.; Sha, J.; Yang, J.; Chen, Y. *Phys. Chem. Chem. Phys.* **2021,** *23,* 22760–22767. doi:10.1039/d1cp03563k
98. Chen, L.; Huang, Z.; Kumar, S. *RSC Adv.* **2014,** *4,* 35852–35861. doi:10.1039/c4ra03585b
99. Chen, L.; Huang, Z.; Kumar, S. *Appl. Phys. Lett.* **2013,** *103,* 123110. doi:10.1063/1.4836995

License and Terms

This is an open access article licensed under the terms of the Beilstein-Institut Open Access License Agreement (https://www.beilstein-journals.org/bjnano/terms), which is identical to the Creative Commons Attribution 4.0 International License (https://creativecommons.org/licenses/by/4.0). The reuse of material under this license requires that the author(s), source and license are credited. Third-party material in this article could be subject to other licenses (typically indicated in the credit line), and in this case, users are required to obtain permission from the license holder to reuse the material.

The definitive version of this article is the electronic one which can be found at:
https://doi.org/10.3762/bjnano.17.86